J. Fluid Mech. (1994), *vol.* 271, *pp.* 173–218

Spiral instabilities in the flow of highly elastic fluids between rotating parallel disks

By JEFFREY A. BYARS[1], ALPARSLAN ÖZTEKIN[1], ROBERT A. BROWN[1] AND GARETH H. McKINLEY[2]

[1] Department of Chemical Engineering, Massachusetts Institute of Technology, Cambridge, MA 02139, USA

[2] Division of Applied Sciences, Harvard University, Cambridge, MA 02138, USA

(Received 19 August 1993 and in revised form 24 January 1994)

Experimental observations and linear stability calculations are presented for the stability of torsional flows of viscoelastic fluids between two parallel coaxial disks, one of which is held stationary while the other is rotated at a constant angular velocity. Beyond a critical value of the dimensionless rotation rate, or Deborah number, the purely circumferential, viscometric base flow becomes unstable with respect to a non-axisymmetric, time-dependent motion consisting of spiral vortices which travel radially outwards across the disks. Video-imaging measurements in two highly elastic polyisobutylene solutions are used to determine the radial wavelength, wavespeed and azimuthal structure of the spiral disturbance. The spatial characteristics of this purely elastic instability scale with the rotation rate and axial separation between the disks; however, the observed spiral structure of the secondary motion is a sensitive function of the fluid rheology and the aspect ratio of the finite disks.

Very near the centre of the disk the flow remains stable at all rotation rates, and the unsteady secondary motion is only observed in an annular region beyond a critical radius, denoted R_1^*. The spiral vortices initially increase in intensity as they propagate radially outwards across the disk; however, at larger radii they are damped and the spiral structure disappears beyond a second critical radius, R_2^*. This restabilization of the base viscometric flow is described quantitatively by considering a viscoelastic constitutive equation that captures the nonlinear rheology of the polymeric test fluids in steady shearing flows. A radially localized, linear stability analysis of torsional motions between infinite parallel coaxial disks for this model predicts an instability to non-axisymmetric disturbances for a finite range of radii, which depends on the Deborah number and on the rheological parameters in the model. The most dangerous instability mode varies with the Deborah number; however, at low rotation rates the steady viscometric flow is stable to all localized disturbances, at any radial position.

Experimental values for the wavespeed, wavelength and azimuthal structure of this flow instability are described well by the analysis; however, the critical radii calculated for growth of infinitesimal disturbances are smaller than the values obtained from experimental observations of secondary motions. Calculation of the time rate of change in the additional viscous energy created or dissipated by the disturbance shows that the mechanism of instability for both axisymmetric and non-axisymmetric perturbations is the same, and arises from a coupling between the kinematics of the steady curvilinear base flow and the polymeric stresses in the disturbance flow. For finitely extensible dumb-bells, the magnitude of this coupling is reduced and an additional dissipative contribution to the mechanical energy balance arises, so that the disturbance is damped at large radial positions where the mean shear rate is large.

Hysteresis experiments demonstrate that the instability is subcritical in the rotation

rate, and, at long times, the initially well-defined spiral flow develops into a more complex three-dimensional aperiodic motion. Experimental observations indicate that this nonlinear evolution proceeds via a rapid splitting of the spiral vortices into vortices of approximately half the initial radial wavelength, and ultimately results in a state consisting of both inwardly and outwardly travelling spiral vortices with a range of radial wavenumbers.

1. Introduction

The torsional motion of a non-Newtonian fluid between coaxial parallel disks is one of the most common geometries employed in rheological measurements. Fluid samples are placed in a narrow gap of height H between two coaxial parallel disks of radius R, and measurements of the torque and normal force exerted by the fluid on the upper plate are used to calculate the shear-rate-dependent material functions of the fluid, as a steady or oscillatory shear flow is driven by rotating the other plate. A key assumption in the subsequent analysis of such measurements, however, is that the flow is always steady and purely azimuthal for all rotation rates. Centrifugal effects, which produce inertial secondary flows in such geometries, are usually negligible because of the high viscosities of most viscoelastic solutions and melts; however, it has recently become clear that secondary flows can develop even in simple geometries at vanishingly small Reynolds number owing to purely elastic instabilities that are entirely absent in the corresponding flows of Newtonian liquids. Such instabilities have been documented in circular Couette flows and Taylor–Dean flows as well as in torsional flows between coaxial disks or between a cone-and-disk, and have recently been reviewed by Larson (1992). Although the detailed mechanism and characteristic features of the elastic instability may vary in each geometry, the driving force in each case is the large difference between the extra normal stresses in the streamwise direction and the direction of shear. This first normal stress difference acts normal to the curvilinear streamlines in the flow and drives a secondary motion. In this paper we provide a detailed experimental and theoretical description of the critical conditions and the spatial form of the instability which develops in the torsional flow of highly elastic model fluids contained between two coaxial disks.

Viscoelastic modifications to the steady, inertially driven, secondary recirculation that is present in confined rotating flows at finite Reynolds numbers have been known to exist since the early observations of Giesekus (1965) and Griffiths, Jones & Walters (1969). Detailed experimental and theoretical studies (Hill 1972; Chiao & Chang 1990) in rotational flows such as the disk-and-cylinder system with low geometric aspect ratios, $(R/H) \sim O(1)$, show that as the rotation rate increases and viscoelastic effects become increasingly important, the weak centrifugal outward motion near the rotating disk reverses direction and becomes directed radially inwards towards the centre of the disks. At still higher rotation rates, time-dependent unsteady motions are observed and calculated.

However, in systems with higher aspect ratios, such secondary motions are typically negligible and the fluid motion is steady and one-dimensional. The first experimental indications of a purely elastic instability in the creeping torsional flow of a viscoelastic fluid were observed by Jackson, Walters & Williams (1984). Measurements of the torque and normal force exerted by a highly elastic polyacrylamide 'Boger fluid' (Boger 1977/78) at high shear rates in a parallel-plate rheometer showed a steady monotonic increase over a period of 20 min. This time-dependent response resulted in

an increase in the apparent viscosity and first normal stress coefficient calculated for the fluid sample, and was interpreted as a time-dependent shear-thickening or anti-thixotropic change associated with the microstructure of the fluid. Subsequent measurements by Magda & Larson (1988) with a number of different Boger fluids containing high molecular weight polystyrene (PS) or polyisobutylene (PIB) showed that the critical shear rate required for the onset of this apparent anti-thixotropic transition was not constant, but varied inversely with the separation H between the plates, and therefore corresponded to an approximately constant critical angular velocity Ω_{crit}. This observation was found to be in good qualitative agreement with calculations performed by Phan-Thien (1983) for the hydrodynamic stability of torsional motions of the upper-convected Maxwell and Oldroyd-B models. In this analysis, Phan-Thien used the von Kármán similarity forms for the velocity and stress fields which are valid when the disks are infinite in extent and examined the linear stability of the base rotational shear flow with respect to disturbances that can also be represented in similarity form. Infinitesimal perturbations were found to grow exponentially in time for values of the Deborah number, $De = \lambda_1 \Omega$, that exceeded the critical value given by $De_{crit} \equiv \pi[(1-\beta)(5-2\beta)]^{-\frac{1}{2}}$. In this expression, λ_1 is the single relaxation time in the constitutive model and $\beta \equiv \eta_s/\eta_0$ is the dimensionless ratio of the solvent viscosity to the total viscosity in the Oldroyd-B model. Hence, the critical rotation rate Ω_{crit} for the onset of this secondary motion is predicted to be a function of the relaxation time and viscosity ratio of the fluid between the plates, but is independent of the gap H between the plates.

Subsequent flow-visualization experiments with another PIB Boger fluid (McKinley *et al.* 1991*a*) showed that a number of the characteristics of this elastic instability cannot be described even qualitatively by the analysis of Phan-Thien. In particular, flow-visualization and dynamic measurements of the shear stress and normal stresses exerted on the plates clearly demonstrated that the flow transition is non-axisymmetric, overstable in time and corresponds to a subcritical bifurcation. Most importantly, the spatial structure of the developing secondary flow consists of a radially periodic structure that scales approximately with the gap H between the plates and not of a single toroidal vortex extending across the entire radial span of the disks, as is expected from perturbations of the similarity form considered by Phan-Thien. As the Deborah number was increased beyond a critical value, these vortices increased in intensity with time and propagated both radially outwards from the centre of the disks and inwards from the free surface at the outer edge of the test geometry. By constructing an experimental stability curve for a number of different aspect ratios R/H and rotation rates, McKinley *et al.* (1991*a*) also showed that the instability is a function of both the rotation rate Ω and the characteristic shear rate $\dot{\gamma}_R \equiv \Omega R/H$ between the plates. This latter variation was attributed to the complex shear-rate-dependence of the viscoelastic material functions of the test fluid studied. It is the quantitative description of this non-axisymmetric, time-dependent flow instability that is the focus of this paper.

It is worth noting that highly elastic fluids, such as polymer melts, also can undergo another, entirely different, type of rotational flow instability known as *edge fracture* in a parallel-plate rheometer (Hutton 1969). Above a critical shear rate, a narrow concave indentation appears in the free surface of the fluid near the midplane between the two disks. This indentation rapidly propagates radially inwards in the form of a crack and the viscoelastic sample is torn into two halves, one attached to each plate. Tanner & Keentok (1983) conjectured that this instability is driven by the negative second normal stress difference $N_2 = (\tau_{zz} - \tau_{rr})$ measured in many polymeric systems. This observation has been verified recently by Lee, Tripp & Magda (1992), who showed that the critical

second normal stress difference N_{2crit} required for edge fracture in one particular cone-and-plate geometry remained almost constant for five different polymer solutions.

Both the purely elastic instability discussed by McKinley *et al.* (1991*a*) and edge fracture can severely limit the operating range of rotational rheometers for polymeric fluids, and the particular ordering of the transitions depends on the relative magnitudes of the first and second normal stress coefficients and the surface tension for a given polymeric fluid. Dilute or weakly entangled polymer solutions, such as the Boger fluids used in our experiments, typically have vanishingly small second normal stress coefficients and are not prone to the edge-fracture instability. In their previous experiments, Lee *et al.* (1992) were not able to observe edge fracture in a polystyrene-based Boger fluid over a wide range of shear rates.

Although inertial transitions and secondary motions in the flow of Newtonian liquids between co- and counter-rotating parallel disks have been the subject of extensive theoretical and experimental attention (see the recent review by Zandbergen & Dijkstra 1987), much less is known about the corresponding flow of viscoelastic fluids. Most of the theoretical analyses have only considered the existence and stability of secondary flows described by the von Kármán similarity form first analysed by Phan-Thien (1983). Walsh (1987) employed a numerical scheme to show the presence of a subcritical bifurcation from the base torsional flow of an upper-convected Maxwell fluid at zero Reynolds number. Similar results showing turning points in dynamic quantities such as the total torque exerted on the plates and the presence of multiple axisymmetric steady-state solutions of similarity form have been found by Ji, Rajagopal & Szeri (1990) for the rotational flow of an Oldroyd-B fluid between infinite co-axial parallel plates at finite Reynolds numbers. Crewther, Huilgol & Jozsa (1991) give a detailed review and mathematical study of both axisymmetric and non-axisymmetric flows for the Oldroyd-B fluid and present examples of some of the hundreds of steady-state solutions they obtained using a bifurcation tracking scheme.

The first analysis that considered disturbances not of the similarity form was presented by Öztekin & Brown (1993) for the inertialess torsional flow of the Oldroyd-B model between infinite parallel plates. These authors considered the linear stability of infinitesimal normal mode disturbances to the base velocity and stress fields of the form

$$F(r, \theta, z, t) = f(z)\, e^{i\alpha r + im\theta + \sigma t}, \tag{1}$$

where F indicates any dimensionless disturbance variable, and all kinematic variables have been non-dimensionalized with the lengthscale H and the timescale Ω^{-1}. In (1) the dimensionless wavenumber α characterizes the radial form of disturbance, and m is an integer describing the azimuthal dependence of the disturbance. Non-axisymmetric instabilities are incorporated by choosing $m \neq 0$. The dimensionless growth rate of the disturbance is given by the complex growth rate $\sigma = \sigma_r + i\sigma_i$. By linearizing the resulting disturbance equations about a critical dimensionless radial location R^*, the authors obtained a separable matrix eigenvalue problem which they solved to find the spatial form of the most unstable disturbance as a function of the local radial position R^*, the Deborah number, De, and the fluid rheology, as measured by the viscosity ratio β. Calculations showed that the most dangerous perturbations led to spiral vortices with positive or negative angle that travelled either radially outwards or inwards, respectively. The critical rotation rate for growth of these disturbances and the azimuthal dependence of the most unstable mode were sensitive functions of the fluid rheology and the local radial position. Most significantly, these disturbances were unstable at large R^* for Deborah numbers considerably below the critical condition predicted by the Phan-Thien analysis, and thus are more likely to be observed

experimentally. The critical radial wavenumber α at the onset of the instability was in good agreement with the few photographs presented by McKinley *et al.*, but quantitative comparison of the azimuthal structure and wavespeed were inhibited by the lack of data. In the current work, we report more extensive flow-visualization observations of the spatial and temporal form of the secondary flow between the plates which enable us to perform a critical comparison with the results of the linear stability analysis.

The calculations of Öztekin & Brown were performed with the quasi-linear Oldroyd-B model which predicts a constant viscosity η_0 and a constant first normal stress coefficient Ψ_{10} in steady torsional shear flows at all rotation rates. However, for Boger fluids such as those used in the experiments of Magda & Larson and McKinley *et al.*, it is well known that although the shear viscosity is almost constant across many decades of shear rate, the first normal stress coefficient is only constant at low shear rates and decreases monotonically even at moderate shear rates (Prilutski *et al.* 1983; Quinzani *et al.* 1990). Despite this limitation, the predicted form of the neutral stability curve obtained by Öztekin & Brown for the critical onset radius as a function of the Deborah number adequately described the experimental measurements of McKinley *et al.* when the effective relaxation time $\lambda_1(\dot{\gamma})$ for the test fluid was evaluated using the viscometric properties measured at the shear rate corresponding to the maximum value of R^* in the experimental apparatus, and this value was subsequently used as the single relaxation time in the Oldroyd-B model.

Since it is the relative magnitude of the first normal stress coefficient $\Psi_1(\dot{\gamma})$ compared to the shear viscosity which provides the driving force for these purely elastic instabilities, Larson (1992) pointed out that shear-thinning phenomena may be expected to have profound stabilizing effects on the bifurcation structure and stability of highly elastic flows. McKinley *et al.* (1991*a*) demonstrated that when the aspect ratio R/H of the plates was increased at a fixed rotation rate, the increasing importance of shear-thinning effects led to a progressive decrease in the amplitude of the ultimate unstable flow developing between the plates. However, to date, few analytical studies of the stabilizing effects of shear-thinning on purely elastic instabilities have appeared, primarily because of the greatly increased complexity of the analysis which results. Phan-Thien (1985) briefly reported on a linear stability analysis for the inertialess torsional motion of a fluid described by the Phan-Thien–Tanner (PTT) constitutive equation between an infinite cone and disk, and showed that whereas the flow of an Oldroyd-B fluid was unstable beyond a critical rotation rate for a particular form of the disturbance kinematics, the corresponding motion of the PTT model was always stable at all Deborah numbers. Larson, Muller & Shaqfeh (1994) considered the effects of shear-thinning in the viscoelastic material functions, the presence of a Newtonian solvent contribution to the viscosity, and the effects of a distribution of relaxation times on the stability of Taylor–Couette flows to axisymmetric disturbances using the K-BKZ model (Bird, Armstrong & Hassager 1987*a*). They showed that each of these effects increased the critical Deborah number for the onset of the purely elastic instability. Comparison with experimental observations gave reasonable agreement; however, the experimentally determined critical conditions were consistently lower than experimental measurements, and it was speculated that the most likely reason for this discrepancy was that the most unstable disturbance is non-axisymmetric. In the current work, we demonstrate similar trends in the parallel-plate geometry and show that in order to even qualitatively describe the spatial form of the torsional elastic instability, it is necessary to incorporate both non-axisymmetric, time-dependent disturbances, as well as shear-rate-dependent fluid rheology.

The experimental apparatus, the rheology of the two test fluids and the form of the constitutive equation used to model the nonlinear viscometric functions are first described in §2. Video-imaging measurements of the spatial structure and evolution of the elastic instability that is observed as a function of Deborah number, aspect ratio and fluid rheology are presented in §3. The previous linear stability analysis for localized non-axisymmetric disturbances developed by Öztekin & Brown (1993) is extended in §4 to incorporate the more realistic fluid constitutive equation. In addition, results are presented for an energy analysis for non-axisymmetric perturbations, similar to the approach initially developed by Joo & Shaqfeh (1991, 1992) for the Oldroyd-B model, to show that the instability develops owing to a coupling between the polymeric stresses in the base torsional flow and the perturbations in the local velocity field. Finally, a critical quantitative comparison of the observed and calculated secondary motions is presented in §5.

2. Experimental

2.1. *Test apparatus*

All of the experimental measurements were conducted in the apparatus shown schematically in figure 1. A cylindrical coordinate system $(\hat{r}, \theta, \hat{z})$ is defined with origin at the centre of the upper, rotating disk. Throughout the text we use the notation of Öztekin & Brown (1993) and choose the plate separation H, and the rotation rate Ω to define characteristic lengthscales and timescales; all variables are then dimensionless unless explicitly identified with carets. The base of the test cell consisted of a smooth, polished Plexiglas sheet supported by four threaded rods which could be independently adjusted to ensure that the Plexiglas sheet was parallel to the upper disk. The position of the upper disk was controlled using a two-axis lathe mount attached to the rigid frame of the geometry, and the separation of the upper disk and the bottom plate was measured to within ± 1 μm using a digital micrometer. Special care was taken to ensure that the upper and lower disks were parallel to within ± 12 μm. The radius of the upper disk was held constant at $R = 40.0$ mm, and gaps of $H = 2.00$ mm and $H = 3.50$ mm were used in the experiments. The choice of plate separations is experimentally constrained, since, for very small separations, it becomes difficult to resolve the spatial structure of the secondary flow that develops in the narrow gap; for very large plate separations, gravity overcomes the wetting forces which pin the fluid at the edge of the disks, and the sample runs out of the rheometer.

Fluid samples were placed between the disk and the transparent lower plate, and excess fluid beyond the edge of the disk was carefully removed to leave a smooth, approximately cylindrical meniscus at the edge of the disks. According to the analysis of Olagunju (1994) and the material properties of the fluids given in §2.3, the maximum surface deflection is only expected to deviate by a maximum of ± 0.10 mm from a right cylinder and inertial secondary flows of von Kármán form can be completely ignored. The steady torsional flow was driven by rotating the upper disk, which was attached to the spindle of a high-torque d.c. gearmotor (Electrocraft E586). The angular rotation rate Ω of the motor was accurately measured by a tachometer and was incremented in small steps (typically $\delta\Omega = 0.52$ rad s^{-1}), until the onset of the instability was observed.

The flow was illuminated and visualized from a mirror placed below the Plexiglas base at an angle of 45°. Two fibre-optic light sources were positioned to illuminate the entire region between the disk and the plate as uniformly as possible, and trace quantities of small plate-like mica particles (Kalliroscope Corp., Groton , MA) were

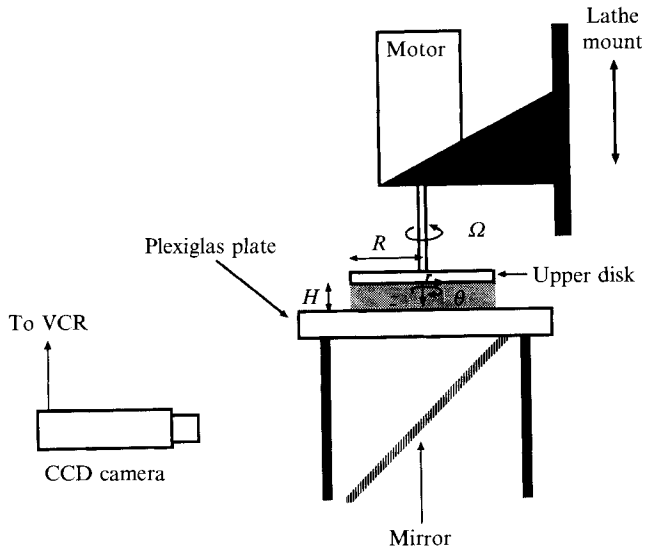

FIGURE 1. Schematic diagram of the parallel plate geometry.

uniformly dispersed into the test fluids in order the increase the visibility of the secondary flow.

Images of the flow were recorded using a high-resolution monochrome CCD camera (COHU 4910) and a Super-VHS video recorder (Panasonic AG1960). Since the analogue gain of the CCD camera is linear, spatial and temporal variations in the intensity of the reflected light by the mica flakes are faithfully recorded as grey-scale variations in the video-images. In §2.2, we explain how these fluctuations can be used to calculate the wavelength and wavespeed of the elastic instability that develops above a critical rotation rate, or Deborah number. Individual images (480×480 pixels) of the entire cross-sectional area of the disk were digitized from each frame of the video-tape using an 8-bit frame-grabber (DIPIX P360), yielding a spatial resolution of ~ 0.18 mm pixel^{-1}. Although flow cells can be readily distinguished visually in the fluid sample and also in the recorded images, a series of image-processing operations was subsequently performed to enhance the visibility of the cells. First, spatial non-uniformities in background light intensity were corrected for by a pixel-by-pixel division of grey-scale values using a prerecorded reference image of the steady flow, as suggested by Russ (1992). The random high-frequency fluctuations in pixel intensity then were smoothed using a low-pass filter with a 5 pixel $\times$ 5 pixel kernel. Finally, the grey-scale histograms of the images were expanded by simultaneously adjusting the contrast and brightness in order to give the best visual definition of the cells. These processed images were analysed to determine the wavenumber, spiral number and wavespeed for each run as described below.

2.2. *Image analysis*

The video-imaging system has been used to make quantitative measurements of the spatial and temporal evolution of the secondary flow that develops in the fluid sample above a critical rotation rate. In order to compare our experimental observations with the results of the linear stability calculations, it is first necessary to understand the relationship between the dimensionless parameters α, m and σ describing the form of the normal mode perturbations considered in the numerical analysis and the

experimental quantities that are actually observable through the transparent base of the rheometer. In our experimental work we have used a classical flow-visualization technique (cf. Merzkirch 1987) based on the addition of anisotropic seeding particles to the viscoelastic test fluid which align with the local direction of the creeping flow between the plates. In a steady two-dimensional flow, the locally-averaged intensity of the reflected light is spatially uniform; however, following the onset of a hydrodynamic instability, spatial and/or temporal variations in the intensity of the reflected light at each point develop and can be used to infer the structure of the developing secondary flow.

Since our observations are limited to two-dimensional images in the (r, θ)-plane of the test cell, the intensity of the reflected light $I(r, \theta, t)$ at any image coordinates (r, θ) fixed with respect to the centre of the stationary base represents an integrated average of the reflections from seed particles moving through that point but distributed over a range of depths z in the fluid. If the observed flow instability is of the normal mode form given by equation (1), then the grey-scale intensity of any pixel in the image obtained from the CCD array is expected to vary as

$$I(r, \theta, t) \propto \overline{f(z)}\, \mathrm{e}^{\mathrm{i}\alpha r + \mathrm{i}m\theta + \sigma t}, \tag{2}$$

where $\overline{f(z)}$ indicates an undetermined weighted z-average of the spatial form of the disturbance to the base flow.

If a pixel is selected in a digitized, two-dimensional image with a maximum intensity I_{max} and we attempt to track points of constant intensity across the image, then the locus of these points at any instant in time will be given by

$$\mathrm{d}I = 0 = \mathrm{i}\alpha\, \mathrm{d}r + \mathrm{i}m\, \mathrm{d}\theta, \tag{3}$$

or by integrating once as

$$r = -\frac{m}{\alpha}(\theta + \theta_0), \tag{4}$$

where θ_0 sets the radial location R_0 of the starting point with respect to the (arbitrary) definition of the line given by $\theta = 0$.

The spatial locations of the recirculating vortices in the secondary flow given by (4) are thus described by *Archimedean Spirals* (Davis 1993) and the winding number of the spiral curves is given by m/α. The radial wavenumber α is only meaningfully defined for positive real numbers and azimuthal periodicity requires that m takes integer values only. If $m > 0$ then the curves spiral inwards towards the origin with increasing θ; if $m < 0$ then the curves spiral outwards. The local spiral angle ϵ may be conveniently defined from (3) as

$$\tan \epsilon = \frac{-\mathrm{d}r}{r\, \mathrm{d}\theta} = \frac{+(m/r)}{\alpha}, \tag{5}$$

and can be interpreted as the ratio of the azimuthal wavenumber (m/r) at any given radius to the radial wavenumber α.

Sample curves are illustrated in figure 2 for a fixed value of radial wavenumber α and increasing values of azimuthal wavenumber $m = 0$, 1 and 2. In each case, the azimuthal coordinate θ is defined from the abscissa $y = 0$ and increases in the clockwise direction. For non-axisymmetric disturbances ($m > 0$), note that although azimuthal periodicity at a fixed radius requires $f(\theta) = f(\theta + 2\pi)$, the locus of each line corresponding to the maximum intensity of a secondary vortex is given parametrically in terms of $0 < \theta < R\alpha/m$. It also should be noted that by following the locus of a single spiral curve it is

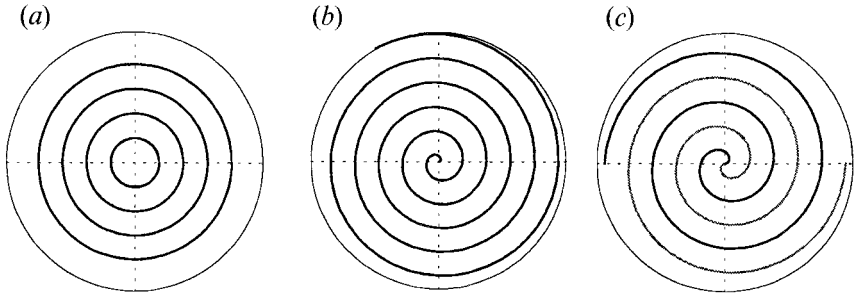

FIGURE 2. Archimedean spirals of the form given by equation (4): (*a*) axisymmetric mode, $m = 0$; (*b*) non-axisymmetric mode, $m = 1$; (*c*) nested non-axisymmetric spirals, $m = 2$. The radial wavenumber α of the spiral is the same in each case.

not possible to determine the values of m and α unambiguously, but only the quotient m/α. The parameter m is determined independently, however, by noting that it indicates the integer number of intertwined, non-intersecting curves that cross a circumferential arc at every radius r.

Video-imaging measurements of variations in the intensity of the reflected light are combined with these equations to determine the parameters describing the spatial form of the instability. The temporal evolution of the secondary flow is quantified by making a sequence of such observations at successive time intervals of $\frac{1}{30}$ s. Profiles of grey-scale intensity as a function of radial position are presented in § 3 and the peaks in the profile are identified as local maxima in the magnitude of the secondary flow. Profiles at a fixed azimuthal position for a sequence of elapsed times show that the instability consists of radially-periodic vortices which travel outwards across the disk. The radial wavenumber α can be calculated from either the Fourier spectrum of a single radial profile $I(r)$, or from the average of all observed peak-to-peak distances at different angular positions. The wavespeed, $c \equiv \mathrm{Im}(\sigma)/\alpha$, of the secondary flow is determined by measuring the position of the centre of each vortex at successive time intervals. Linear regression using (4) of a series of radial intensity profiles at different azimuthal angles θ in an image makes it possible to determine if the secondary flow is axisymmetric or three-dimensional. Information describing the temporal structure of the elastic instability at a single fixed point in space might be obtained from a time-series of LDV measurements (cf. McKinley *et al.* 1991*b*; Muller, Shaqfeh & Larson 1993); however, such observations fail to yield the global spatial form of the instability at any instant in time, so we have not pursued this approach here.

2.3. *Fluid rheology*

Two different Boger fluids have been used in these experiments in order to investigate the effects of variations in the fluid rheology on the flow instability. The first fluid, 0.31 wt% polyisobutylene (Exxon Vistanex L-120, MW $\sim 1.8 \times 10^6$ g mol^{-1}), 4.83 wt% tetradecane (C14) and 94.86 wt% polybutene (Amoco H100, MW $\sim$ 900 g mol^{-1}), is the same as used by McKinley *et al.* (1991*a*). The second fluid consists of a lower concentration (0.20 wt%) of the identical polyisobutylene, dissolved in a more viscous solvent consisting of 3.80 wt% C14 and 96.00 wt% of another polybutene grade (Amoco H300, MW $\sim$ 1300 g mol^{-1}). The zero-shear-rate viscometric properties (η_0, Ψ_{10}) and the associated model parameters for the Oldroyd-B constitutive equation for each of the two fluids are given in table 1. The lower concentration of identical molecular weight polymer in the 0.20 wt% Boger fluid

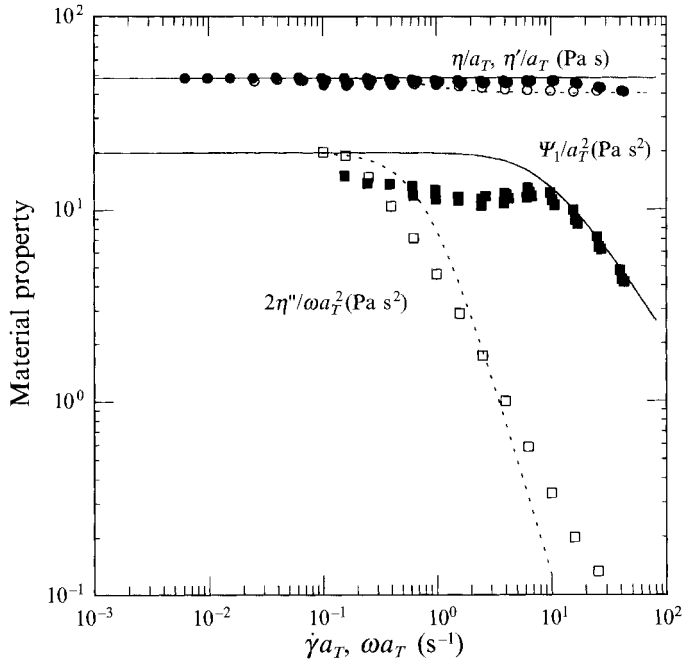

FIGURE 3. Viscous and elastic material functions for the 0.2 wt% PIB fluid at 25 °C. Solid symbols are steady shear flow properties: ●, viscosity η [Pa s]; ■, first normal stress coefficient Ψ_1 [Pa s^2]. Hollow symbols are linear viscoelastic properties: ○, dynamic viscosity η' [Pa s] and □, $2\eta''/\omega$ [Pa s^2]. The predictions of the steady shear properties of a single-mode Chilcott–Rallison model with $\eta_0 =$ 48.1 Pa s, $c = 0.20$, $\lambda_1 = 1.24$ s and $L = 20$ also are shown.

		0.31% PIB/H100	0.20% PIB/H300
η_0	[Pa s]	13.76	48.1
η_s	[Pa s]	8.12	40.1
Ψ_{10}	[Pa s^2]	8.96	19.8
λ_1	[s]	0.794	1.24
β		0.59	0.84

TABLE 1. Visometric properties of the two polyisobutylene (PIB) test fluids used in the experimental observations of the torsional flow instability.

results in a lower polymeric contribution to the total viscosity, and thus a higher value of the solvent viscosity ratio $\beta \equiv \eta_s/\eta_0$. For dilute, or semi-dilute solutions such as these Boger fluids, the longest relaxation time depends on the concentration and molecular weight of the polymeric solute, the polymer–solvent thermodynamic interactions and the viscosity of the solvent that the chains are dissolved in (Ferry 1980). Since the same polyisobutylene is used in both fluids and the chemical composition of the surrounding solvent is essentially unchanged (in both cases the solvent is essentially *athermal*; Flory 1953), the lower concentration of the polymer in the 0.20wt% fluid is outweighed by the significantly higher solvent viscosity of the H300 polybutene, resulting in a larger first normal stress coefficient and a longer fluid relaxation time. The temperature dependence of the material properties of these fluids for 9 °C $< T <$ 40 °C is described by an Arrhenius equation with flow activation

energies of $\Delta H = 61.2$ kJ and 62.0 kJ, respectively. A change of 1 °C in the fluid temperature results in an 8% change in the fluid viscosity and relaxation time, and it is therefore crucial to carefully monitor the ambient temperature and adjust the material functions appropriately. Experiments were conducted between 22 °C and 26 °C, and we report critical conditions corrected to a reference temperature of 25 °C.

The rheology of the 0.31 wt% fluid has been presented extensively elsewhere (Quinzani *et al.* 1990), therefore only the steady-shear rheology of the 0.20 wt% PIB fluid is presented in figure 3. The shear viscosity η of the solution is almost constant across four decades of shear rate owing to the high underlying viscosity of the Newtonian solvent. The first normal stress coefficient asymptotically approaches a constant value Ψ_{10} at low shear rates, indicating quadratic growth of the first normal stress difference; however, at intermediate shear rates, significant shear-thinning in $\Psi_1(\dot{\gamma})$ becomes apparent. The complex plateau behaviour of $\Psi_1(\dot{\gamma})$ is characteristic of almost all Boger fluids (Quinzani *et al.* 1990), but cannot be captured by the simple quasi-linear Oldroyd-B model which predicts a shear-rate-independent value of the first normal stress coefficient. The magnitude of the spatial gradients in the first normal stress difference plays a dominant role in the onset of purely elastic instabilities (Joo & Shaqfeh 1992; Öztekin & Brown 1993), and the shear-rate-dependence of $\Psi_1(\dot{\gamma})$ may be expected to significantly affect the stability boundaries of the base rotational shear flow. In order to model this nonlinear fluid rheology we have selected the constitutive equation proposed by Chilcott & Rallison (1988) and the predictions of the model are also shown in figure 3. In this constitutive model, the PIB molecules are considered to be a dilute solution of non-interacting dumb-bells with dimensionless concentration c, dissolved in a Newtonian solvent of viscosity η_s. The two beads of the dumb-bell are connected by a nonlinear elastic spring with a finite maximum extensibility L, which represents the ratio of the fully extended length of the dumb-bell to its r.m.s. length at equilibrium. By eliminating the second-rank tensor describing the configuration of the dumb-bells from the original equations of Chilcott & Rallison, the constitutive equation for the polymeric contribution to the stress $\hat{\boldsymbol{S}}$ can be written simply as

$$\hat{\boldsymbol{S}} + \lambda_1 \left(\frac{\hat{\boldsymbol{S}}}{f}\right)_{(1)} = \eta_p \dot{\boldsymbol{\gamma}}, \tag{6}$$

where λ_1 is the single time constant in the model, $f \doteq (L^2 + (\lambda_1/\eta_p)\,\mathrm{tr}(\hat{\boldsymbol{S}}))/(L^2-3)$ is a measure of the nonlinearity in the spring connecting the dumb-bells, and η_p is the polymeric contribution to the viscosity. The dimensional shear-rate tensor is given by $\dot{\boldsymbol{\gamma}} \equiv (\boldsymbol{\nabla}\hat{\boldsymbol{u}})^T + \boldsymbol{\nabla}\hat{\boldsymbol{u}}$. The solvent is Newtonian with constitutive equation $\hat{\boldsymbol{\tau}}_s = \eta_s \dot{\boldsymbol{\gamma}}$, and the total stress tensor is given by the linear combination $\hat{\boldsymbol{\tau}} = \hat{\boldsymbol{\tau}}_s + \hat{\boldsymbol{S}}$.

In the limit $L \to \infty$, the dumb-bells become infinitely extensible and (6) simplifies to the upper-convected Maxwell model; the constitutive equation for the total stress tensor $\hat{\boldsymbol{\tau}}$ is then equivalent to the Oldroyd-B model (Bird *et al.* 1987*b*). However, for finite values of L, the model predicts the onset of shear-thinning in the first normal stress coefficient beyond dimensionless shear rates of $\lambda_1 \dot{\gamma} \cong L^2/(8(L^2-3))^{\frac{1}{2}}$ with an asymptotic decrease at high shear rates which scales as $\Psi_1(\dot{\gamma}) \sim \dot{\gamma}^{-1}$. The steady-shear viscosity of the model remains constant with a value $\eta_0 \equiv \eta_s + \eta_p$ and the polymeric contribution to the viscosity depends on the concentration of dumb-bells as $\eta_p \equiv \eta_s c$. At high shear rates, the apparent relaxation time $\lambda_1(\dot{\gamma}) \equiv \Psi_1(\dot{\gamma})/2\eta_p(\dot{\gamma})$ of the model decreases monotonically from the value of

$$\lambda_1 \equiv \lim_{\dot{\gamma} \to 0} \lambda_1(\dot{\gamma})$$

determined from the zero-shear-rate viscometric properties. In order to distinguish carefully between these two relaxation times, we define a Deborah number based on the zero-shear-rate relaxation time λ_1 appearing in (6) as $De_0 \equiv \lambda_1 \Omega$, and a second, shear-rate-dependent quantity based on the local apparent shear rate as $De(\dot{\gamma}) \equiv \lambda_1(\dot{\gamma})\Omega$.

The dimensionless concentration c of the dumb-bells appearing in the model is determined directly from the measured zero-shear-rate viscosities and the solvent viscosities given in table 1. The single remaining model parameter L is determined independently by fitting the form of the shear-rate-dependent first normal stress coefficient at high shear rates. Since the same molecular weight PIB molecules are used in both fluids and the nature of the polymer–solvent interactions are almost unchanged, very similar values of the extensibility should describe both the 0.31 wt% and the 0.20 wt% Boger fluids. By constraining the model to describe more closely the viscometric data at high shear rates of $\dot{\gamma} \geqslant 10\ \mathrm{s}^{-1}$ as shown in figure 3, the best estimate value of $L = 20$ is obtained for the 0.20 wt% PIB fluid. Previous work (McKinley, Armstrong & Brown 1993) used a value of $L = 12$ to model the shear-rate-dependence of the 0.31 wt% fluid. The slight discrepancies between these values of L can be attributed to intermolecular interactions between polymer chains which are neglected in the dilute-solution theory, but which may be significant in the semi-dilute Boger fluids. A more robust method of determining the extensibility would be via measurements of the extensional viscosity of each solution, if such data were available. In uniaxial elongation, the Chilcott–Rallison model predicts significant extensional thickening with an asymptotic extensional viscosity that scales as $O(cL^2)$.

Like other dilute-solution dumb-bell models, the Chilcott–Rallison model predicts a zero value of the second normal stress coefficient Ψ_2 at all shear rates. Although we have not determined Ψ_2 for the two Boger fluids used in this study, measurements by Magda and coworkers for other PIB and PS-based Boger fluids indicate that, within experimental error, the second normal stress coefficient is indeed zero (Magda *et al.* 1991; Lee *et al.* 1992). Non-zero negative values of Ψ_2 are predicted to stabilize purely elastic instabilities in other curved geometries (Shaqfeh, Muller & Larson 1992), but induce edge-fracture instabilities in cone and plate and parallel-plate flows (Larson 1992). Boger fluids are thus ideally suited for experimental studies of the elastic flow instability between parallel plates, in the absence of edge disturbances.

The linear viscoelastic properties $(\eta', 2\eta''/\omega)$ of the 0.20 wt% fluid determined by small-amplitude oscillatory motions of the parallel disks also are shown in figure 3. The discrepancy between the experimental data and the predictions of the single-mode Chilcott–Rallison model, which reduces to the same form as the Oldroyd-B model in the limit of small strains, serves to emphasize that a spectrum of time constants is required for a quantitative description of the material properties of even simple 'model systems' such as Boger fluids in transient shear flows over a range of deformation (Bird *et al* 1987*a*).

Despite this shortcoming, this simple nonlinear constitutive model allows systematic evaluation of the effects of variations in the fluid rheology on the spatial form of the torsional flow instability. In their analysis of the purely elastic instability that arises in Taylor–Couette flows of the K-BKZ model, Larson *et al.* (1994) found that shear-thinning led to an increase in the critical Deborah number for the onset of the instability. Although the cellular form of the instability remained the same, the spatial wavenumber was observed to depend on the degree of shear-thinning. However, in the limit of very narrow gaps, the Taylor–Couette flow is homogeneous and the shear rate across the narrow annular gap of a circular Couette cell is constant; fluid elements at different radial locations therefore are described by the same material properties. In

contrast, the torsional motion between parallel disks considered in this work is an inhomogeneous shear flow, and the local shear rate increases linearly with radial position from zero at the centre to a maximum value $\dot{\gamma}_R = \Omega R/H$ at the edge of the disks. If a test fluid exhibits shear-thinning, then the viscoelastic material properties, and thus the local stability of the base flow, will vary radially across the disk even at a fixed rotation rate.

The local ratio of the first normal stress difference to the shear stress at any radial position is defined as a *stress ratio* $S_r \equiv \Psi_1(\dot{\gamma})\dot{\gamma}/\eta(\dot{\gamma})$. When the shear rate at the edge of the disks is taken as a characteristic deformation rate for the flow, this stress ratio is often referred to as a *Weissenberg number* (McKinley *et al.* 1991*a*; Larson 1992). For the Oldroyd-B model the stress ratio increases radially outwards in a linear manner, and the previous linear stability analysis of Öztekin & Brown demonstrates that for all radial positions greater than a critical value the flow will be unstable to non-axisymmetric disturbances. As the rotation rate increases, the value of the stress ratio at any radial position increases, and the critical onset point of the instability shifts to smaller radial positions. However, if the viscosity and first normal stress coefficient are shear-rate-dependent, then the stress ratio no longer increases linearly across the disk. In fact, for the Chilcott–Rallison model considered in this work, it asymptotically approaches a constant value of $(2(L^2-3))^{\frac{1}{2}}$ at large radii. This spatial variation in the gradients of the local stress ratio coupled with the curvature of the fluid streamlines is shown in §§3 and 4 to result in a spatially localized unsteady flow that only extends across a finite annular region of the disks.

3. Experimental results

Experimental observations are presented which allow the determination of the spatial and temporal characteristics of the purely elastic torsional flow instability. The consequences of the flow instability on the total torque and thrust exerted by the fluid on the plate are demonstrated in §3.1, and the limitations of the data that can be obtained from such spatially-averaged measurements are summarized. A detailed analysis of the spatial and temporal evolution of the flow instability in the 0.31 wt% Boger fluid for a fixed geometric aspect ratio of $R/H = 20$ is presented in §3.2, and the spiral parameters describing the local form of the non-axisymmetric disturbance are determined. The effects of changing fluid rheology and aspect ratio on the instability are shown in §3.3. Observations of a second flow transition that develops at later times from well-defined spiral vortices of a single spiral number to a complex nonlinear state composed of non-axisymmetric disturbances with a spectrum of radial wavelengths are described in §3.4.

3.1. *Dynamic torque and normal force measurements*

Previous measurements of the onset of the torsional flow instability typically have been limited to dynamic measurements of the total torque $\mathscr{T}$ and the total thrust, or normal force, $\mathscr{F}$ exerted on the stationary upper disk of a commercial parallel-plate rheometer as the lower disk is rotated at various speeds (Magda & Larson 1988; Steiert & Wolff 1990; McKinley *et al.* 1991*a*). Typical results are presented in figure 4 for the apparent first normal stress difference, $N_{1a}(t) = 4\mathscr{F}(t)/\pi R^2$ measured in the 0.20 wt% PIB Boger fluid during the start-up of steady shear flow in a Rheometrics RMS-800 Mechanical Spectrometer. The sensitive dependence of the instability on the angular rotation rate Ω between the plates is clearly observed. In each experiment, a fresh fluid sample is used, the rotation rate is increased, and the aspect ratio R/H between the plates is

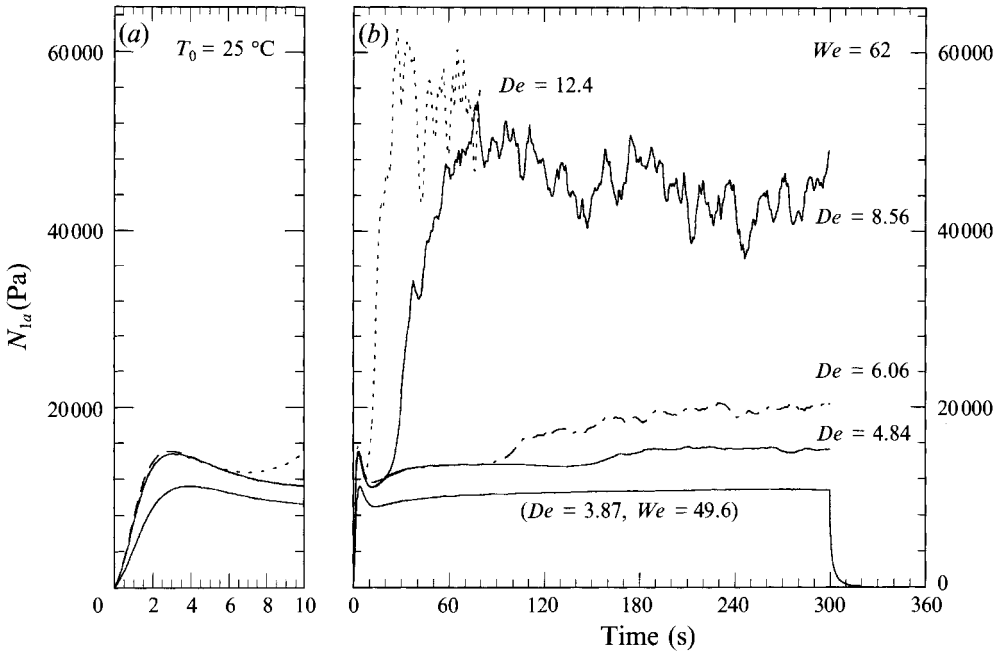

FIGURE 4. Transient response of the apparent first normal stress difference of the 0.20 wt % PIB fluid in a parallel plate rheometer: (*a*) initial overshoot and (*b*) growth of the instability as a function of Deborah number for a constant Weissenberg number *We*.

decreased proportionately, such that the rim shear-rate and thus the Weissenberg number of the flow remains fixed. At short times, N_{1a} grows quadratically, passes through a local maximum and then decreases towards a steady asymptotic value, as shown in figure 4(*a*). The initial transients superpose for all experiments performed at the same shear rate (or Weissenberg number), regardless of the rotation rate or Deborah number of the flow, as expected from the fundamental rheological premise that the material properties of a simple fluid are a unique function of the local deformation rate. For low values of the rotation rate, the first normal stress difference smoothly asymptotes to the expected steady-state value and subsequently remains constant at all future times. However, as the rotation rate is increased beyond a critical value of $\Omega_{crit} = 3.90$ rad s^{-1}, the normal stress exhibits a rapid increase above the expected steady-state value to a final time-dependent state. We show in §3.2 that these complex aperiodic fluctuations correspond to the onset and nonlinear evolution of a non-axisymmetric secondary flow between the plates. The magnitude of this transient increase in the normal stress N_{1a} becomes larger, and the induction time for onset of the instability becomes progressively shorter as the rotation rate and Deborah number are increased. Similar behaviour is observed in the torque exerted by the fluid on the plate. In our earlier work (McKinley *et al.* 1991*a*) a series of such measurements was used to show that the initial growth in the stresses is exponential in time, that there is hysteresis in the flow and thus that the instability is subcritical in rotation rate. However, because the measured thrust and torque correspond to integrated values of the actual stresses acting on the plate at each point, it is not possible to deduce information about the spatial form of the instability. We do not pursue such measurements further in the current work.

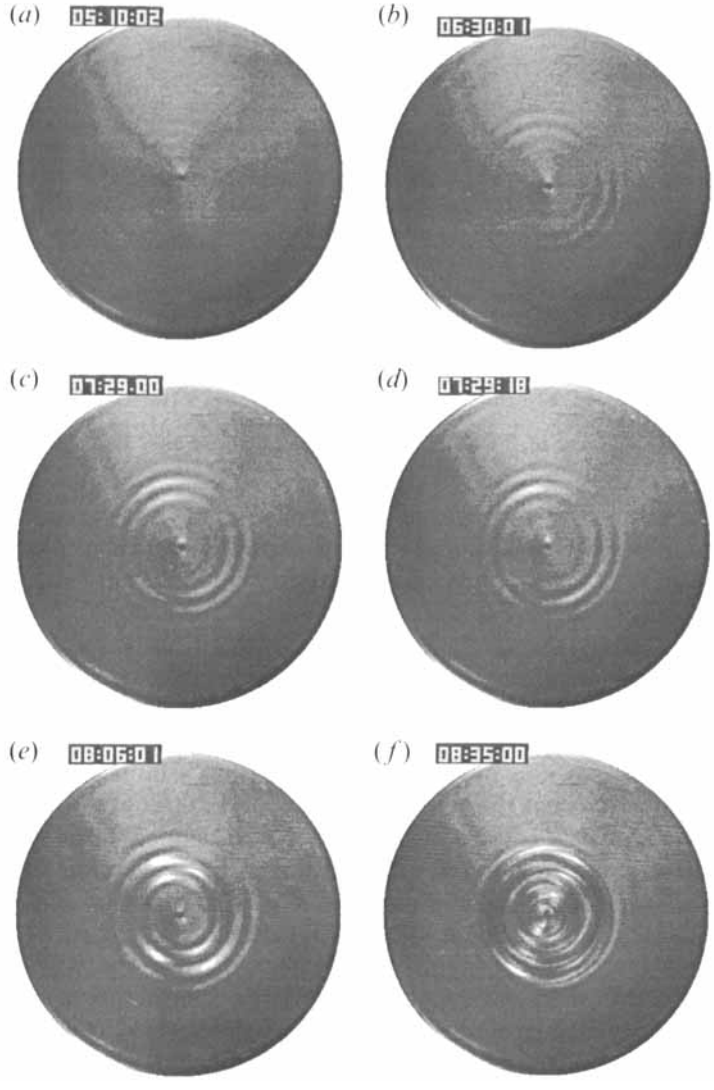

FIGURE 5. Onset and growth of the purely elastic instability observed in the torsional flow of the 0.31 wt % PIB fluid between coaxial parallel disks with $R/H = 20$: (*a*) flow appears stable shortly after the Deborah number is increased to $De_0 = 5.99$ at $\hat{t} = 5{:}00{:}00$ (min:s:frame); (*b*) after an induction time of 90 s, the spatial structure of the secondary flow becomes visible; (*c–d*) outward-travelling non-axisymmetric secondary flow consisting of a single spiral vortex; (*e*) nonlinear mode interaction; (*f*) ultimate fully nonlinear state.

3.2. *Non-axisymmetric disturbances of spiral form*

A series of observations depicting the evolution of the kinematics in the torsional flow were made using the 0.31 wt % fluid with a fixed plate separation of $H = 2.00$ mm, corresponding to an aspect ratio of $R/H = 20$. The series of grey-scale images shown in figure 5 were obtained using the video-imaging system described in §2.1 and depict the spatial and temporal evolution of the flow at a fixed rotation rate as it progresses from the stable base flow (*a*), through a well-defined spatially periodic spiral structure (*b–d*) before ultimately developing into a nonlinear state with many modes present (*e–f*). A steady rotational flow is initially established between the plates at a rotation

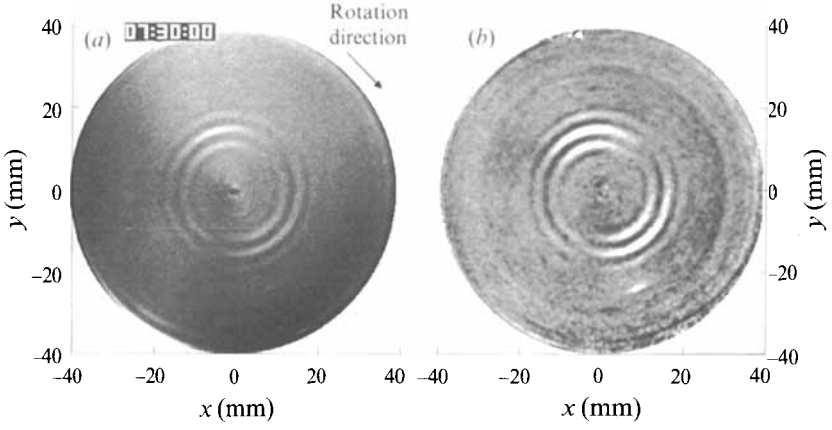

FIGURE 6. (*a*) Raw image of the flow instability and (*b*) enhanced image showing the spiral structure of secondary flow. $De_0 = 5.99$, $Re = 0.032$.

rate below the critical value Ω_{crit} and the flow is observed for 5 min or more to ensure that it is stable; this corresponds to the intensity of the light reflected by the seed particles being uniform across the disk. At time $\hat{t} = 5{:}00{:}00$ (min:s:frame), the rotation rate is incremented to a slightly supercritical value, corresponding to $De_0 = 5.99$. The flow field shown in figure 5(*a*) is already unstable, and measurements of the torque and normal force on the disks indicate that the initially small changes in the stresses arising from the secondary flow are growing exponentially. After 90 s, the secondary flow has grown in intensity sufficiently that a faint spiral structure can be discerned in figure 5(*b*) near the centre of the disk. The strength of the secondary flow continues to increase and after another 60 s, a well-defined spiral secondary flow is clearly visible in figure 5(*c*). Direct observation of the videotape clearly shows that these spiral vortices travel steadily outwards across the disk but remain confined to a narrow annular ring. The secondary flow structure shown in figure 5(*d*) was observed 0.60 s (18 video frames) after figure 5(*c*), at which time the vortices have moved outward by about half their wavelength. Quantitative measurements of the wavelength, wavespeed and azimuthal structure characterizing this instability are presented below. At longer times nonlinear interactions become important, and the periodic spatial structure of the secondary flow begins to become less well-defined, as shown in figure 5(*e*). Dynamic measurements indicate that the increases in the forces exerted on the plates owing to the secondary flow begin to saturate at this time. Ultimately, the secondary flow becomes highly nonlinear with a wide spectrum of spatial structure present, as shown in figure 5(*f*). This non-axisymmetric time-dependent flow will persist until either the torsional motion is completely stopped, or the rotation rate is reduced below a second, lower critical value for return to the steady-state torsional flow. Some evidence of polymer degradation is observed after long periods in the unstable state, as discussed by McKinley *et al.* (1991*a*).

In order to quantify the secondary flow, it is necessary to enhance the visibility of the structures observed in the sequences of video images, such as those shown in figure 5. Typical raw and postprocessed images are presented in figure 6 after application of the image processing operations described in §2.1. Correcting for the non-uniform background illumination increases the azimuthal visibility of the cellular structure around the entire disk, while adjusting the brightness and contrast expands the histogram of grey-scale values present to yield enhanced visual definition of the cells.

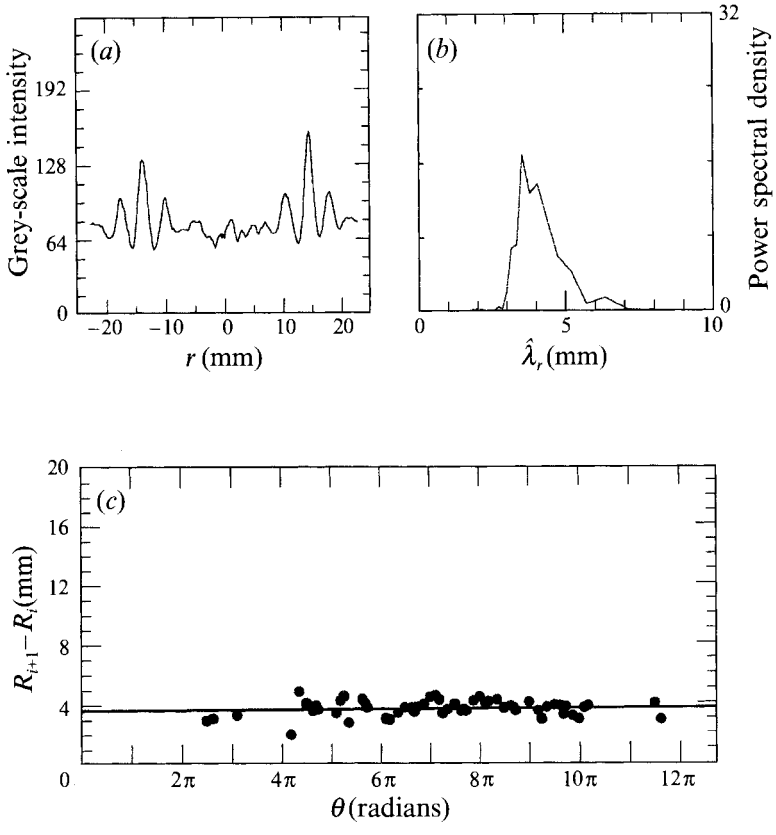

FIGURE 7. Data for the calculation of the radial wavelength of the secondary flow shown in figure 6. (*a*) Radial profile along $\theta = -1.00$ rad; (*b*) Fourier spectrum of radial intensity fluctuations; $\hat{\lambda}_r = 3.57 \pm 0.12$ mm (*c*) average distance between the peaks in figure 10; $\overline{\Delta R} = 3.66 \pm 0.53$ mm, $De = 5.99$, $We = 120$.

However, as is clear from an examination of figure 6, these operations do not compromise the fidelity of the spatial variation in the secondary flow structure.

A Cartesian coordinate system is superimposed on the digitized images of the secondary flow with its origin at the centre of the disk, as shown in figure 6, and the cylindrical coordinate system required for definition of the spiral disturbance forms discussed in §2.2 is located with the line $\theta = 0$ aligned along the positive x-axis, and angles increasing in the direction of rotation of the upper plate. For all the experimental results presented here, θ increases in the clockwise direction. The radial structure of the instability is determined by measuring grey-scale variations in the intensity of the light reflected by the seeding particles in the flow along any radial line passing through the origin, as demonstrated in figure 7(*a*) for the radial line corresponding to $\theta = -1.00$ rad. In this profile and all others presented in this work, the negative radial coordinates indicated on the abscissa indicate distances along the radial line given by extending $\theta \rightarrow \theta + \pi$ rad.

The radial wavelength of the secondary flow can be calculated from such profiles in a number of ways. A Fourier transform of the intensity profile yields the power spectrum shown in figure 7(*b*) and the radial wavelength is determined as $\hat{\lambda}_r = 3.57 \pm 0.12$ mm, corresponding to a dimensionless radial wavenumber of $\alpha = 3.52 \pm 0.12$. Alternatively, the radial separation between each pair of adjacent peaks in

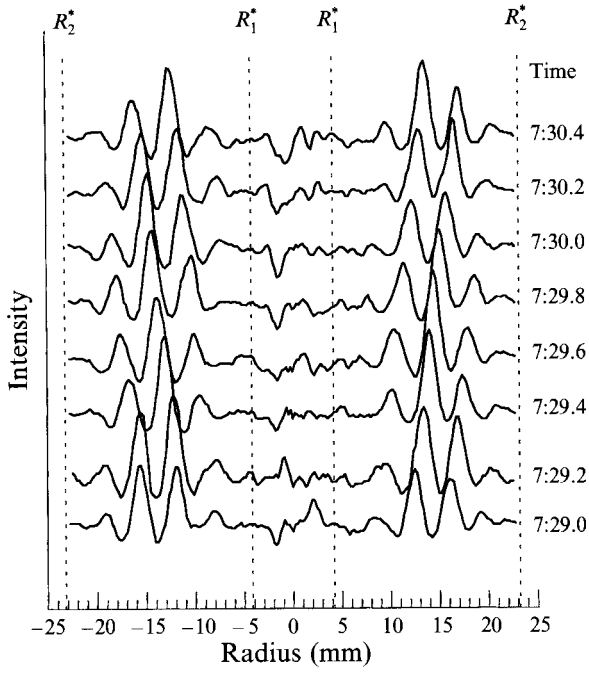

FIGURE 8. Temporal evolution of radial intensity profiles along a fixed line of $\theta = -1.00$ rad. The scale is vertically offset for each profile to show the movement of the cells. The line $\theta = 0$ is along the line $y = 0$, $x > 0$ in figure 6. The timescale is indicated in min:s.

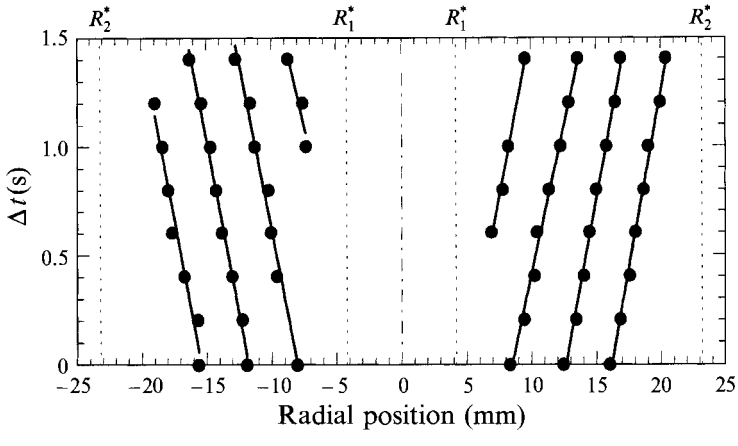

FIGURE 9. Positions of the peaks measured from the profiles of figure 8 as a function of elapsed time. The wavespeed is calculated as 3.18 ± 0.27 mm s^{-1}.

the intensity profile is calculated as a function of the angular position as shown in figure 7(*c*). From such measurements, the radial wavelength is found to be almost constant at different azimuthal positions with an average value and standard deviation determined from figure 7(*c*) as $\hat{\lambda}_r = 3.66 \pm 0.53$ mm.

The temporal evolution of the flow is determined unambiguously from a sequence of radial intensity profiles along a line of constant θ, as shown in figure 8 for the same angular position of $\theta = -1.00$ rad. The elapsed times given in figure 8 are the same as those in figure 5, and the intensity of each profile has been vertically offset for clarity.

These profiles clearly show the travelling-wave structure of the secondary flow. At any given instant in time, the disturbance appears radially periodic and the intensity of the secondary flow passes through a maximum with increasing $\hat{r}$. The centre of each vortex moves radially outward with time; the growth and ultimate decay of the disturbance can be followed by following the location of a particular crest as a function of time. The smallest dimensionless radius at which an intensity peak can be detected is denoted as R_1^*, and the largest radius at which the peaks are still distinguishable is denoted as R_2^*. The irregular fluctuations in the baseline intensity near the centre of the disk are caused by an imperfect match between the background reference image and each successive image of the instability. These fluctuations are present even between successive images of the uniform base flow at subcritical rotation rates and typically arise because of small inhomogeneities in the flow, such as minute air bubbles, which are difficult to eliminate and which migrate to the region of low shear near the centre of the disks.

The radial position of each successive peak in the intensity profiles shown in figure 8 is determined for each timestep, and is replotted in figure 9 as a function of time. Linear regression through each series of points yields the wavespeed of the instability. The radial component of the wavespeed is determined as $\hat{c}_r = 3.18 \pm 0.27$ mm s^{-1}, equivalent to a dimensionless value of $c_r = 0.23 \pm 0.02$.

It is immediately apparent from figure 7(*a*) that the secondary flow is non-axisymmetric, because the peaks in the intensity profiles are located at different radial positions on either side of the origin. However, from closer consideration of (4) and figure 2, it is clear that this single profile can only be used to determine that the disturbance, if of spiral form, does not correspond to an even value of the integer spiral number m. In order to precisely determine the non-axisymmetric structure of the instability, similar measurements of the radial structure are required across the disk at different angular positions. As previously noted, the spiral number m only appears in (4) in the product m/α. Analysis of the data proceeds by selecting a trial value of m, and combining this with an initial guess for the value of α taken from the independent measurements shown in figure 7. Linear regression of the experimental data with (4) then yields best-fit values of α^{-1} and θ_0 for a given value of m. Selection of the Archimedean spiral which most closely describes the overall spatial form of the flow is then based on the data regression which results in the highest correlation coefficient. For the flow of the 0.31 wt% fluid between parallel plates with an aspect ratio of $R/H = 20$, the spatial structure of the secondary flow is best described by an outwardly travelling spiral of positive angle ($m = 1$) with a dimensionless radial wavenumber $\alpha = 3.64$. Figure 10(*a*) shows the positions of the intensity maxima of the digitized image superimposed on a raw image of the secondary flow. Figure 10(*b*) shows the same data as figure 10(*a*), but with the spiral curve representing the instability 'unwrapped' in the θ-direction to demonstrate more clearly how well this form of the disturbance can describe the experimentally observed non-axisymmetric flow. For $m > 1$, there would be m different curves corresponding to m intertwined spiral vortices, each offset by an angular displacement of $2\pi/m$.

The quantitative values of the wavespeed, wavelength and azimuthal structure of the instability also compare well with the linear stability analysis of Öztekin & Brown (1993). If the apparent relaxation time of the fluid is evaluated at the local shear rate of $\dot{\gamma} = 16$ s^{-1} corresponding to the onset radius R_1^*, then the local shear-rate-dependent Deborah number is $De(\dot{\gamma}) \approx 2.8$. At this Deborah number, the most unstable mode is predicted by Öztekin & Brown to be a non-axisymmetric disturbance with $m = 1$, a wavespeed of $c_r = 0.24$ and a wavenumber $\alpha = 3.13$.

Although the experimentally observed secondary flow consists of spiral vortices

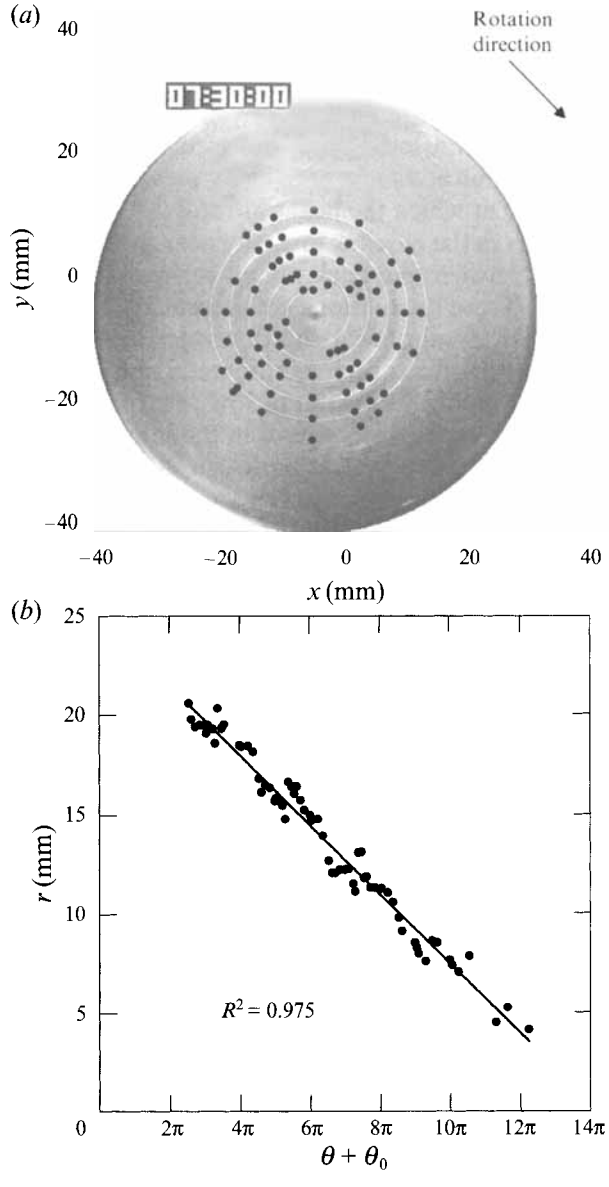

FIGURE 10. (*a*) Positions of the peaks determined from intensity profiles at different azimuthal positions superimposed on a video image of the flow. (*b*) Positions of the peaks with the best fit of equation (4) to these positions with $m = 1$, $\hat{\alpha} = 1.80\ \text{mm}^{-1}$ and $\theta_0 = 0.435$ rad.

which propagate radially outwards, it should be noted that they do not initiate at the centre of the disks nor do they travel completely out of the edge of the fixtures. Rather, the vortices start at a finite radius, grow and then decay to zero amplitude at some second larger radial position, and are only visible for radial positions in the range $4.2\ \text{mm} < \hat{r} < 23.2\ \text{mm}$, corresponding to dimensionless positions of $2.1 < r < 11.6$. This is in sharp contrast to the predictions of the linear stability analysis for an Oldroyd-B fluid, which predicts that the torsional flow is linearly unstable to spiral disturbances of the same form as observed here for all radii greater than a single critical radius $R^* = R^*_{crit}$. An explanation of this difference is presented in §4.2 where an

β	R/H	De_{0crit}	$\dot{\gamma}_R$ [s^{-1}]	$\hat{\lambda}_r$ [mm]	R_1^*	R_2^*	α	c_r	m
0.59	20.0	5.99	151	3.45	2.1	11.6	3.64	0.23	1
0.59	11.4	6.35	91	5.94	3.3	11.2	3.70	0.23	0
0.84	20.0	5.85	94	3.06	1.1	8.8	4.11	0.21	2
0.84	11.4	6.18	57	5.46	2.7	9.5	4.03	0.21	1

TABLE 2. Critical conditions for the onset of the rotational flow instability for two different viscoelastic PIB/PB/C14 test fluids.

energy analysis for the shear-thinning constitutive model describing the fluid shows that the onset radius observed in figure 5 corresponds to the point at which the radial gradients in the normal stresses coupled to the curvilinear streamlines lead to growth of perturbations in the velocity field. These disturbances subsequently decay beyond a second critical radius owing to shear-thinning of the first normal stress difference, which reduces the relative importance of the elastic effects in the flow.

3.3. *Effect of aspect ratio and fluid rheology*

The linear stability analysis of Öztekin & Brown for the Oldroyd-B fluid indicated that the spatial form of the instability scaled with the gap separation H between the parallel plates and that the loci of the neutral stability curves were sensitive functions of the dimensionless solvent viscosity ratio β. Sets of experiments similar to those described in §3.2 have been performed for the two different PIB Boger fluids described in §2.3 using two different representative aspect ratios. The results from these experiments are summarized in table 2. The two fluids are differentiated in table 2 and the subsequent text by their respective values of the solvent viscosity ratio, which are $\beta = 0.59$ for the fluid containing 0.31 wt% PIB, and $\beta = 0.84$ for the 0.20 wt% fluid.

In each fluid, enlarging the separation between the plates and decreasing the aspect ratio R/H results in a small increase in the critical Deborah number required for onset of the elastic instability. However, for the smaller aspect ratio of $R/H = 11.4$, the shear rate at the edge of the disk, and thus the Weissenberg number at the onset of the flow instability, is actually lower. This is in good agreement with our earlier experimental and theoretical findings. For a larger gap, the local shear rate at any radial position across the plates at onset is lower and shear-thinning effects are less important. Consequently, the spatial extent of the secondary flow extends almost completely out to the edge of the disks. The dimensional wavelength and wavespeed both increase as the gap is increased; however, the dimensionless wavenumber α (scaled with the gap H) remains almost unchanged, as expected from the analysis of Öztekin & Brown. The wavespeed also scales well with gap size, and is in excellent agreement with the value predicted for the Oldroyd-B model using the shear-rate-dependent relaxation time.

For the $\beta = 0.59$ fluid, an axisymmetric instability consisting of concentric vortices which travel radially outwards across the disk is observed for an aspect ratio of $R/H = 11.4$. Although Öztekin & Brown predict that the $m = 1$ mode should still be the most unstable mode at these conditions, the spacing in the stability curves for different m is very small, and the $m = 0$ mode is just slightly more stable at this De. The linear stability analysis yields neutral stability curves along which the temporal growth rate of the instability is zero and does not predict which finite-amplitude states will be observed at supercritical conditions. Such results must be found from a nonlinear analysis.

The Deborah number at the onset of the instability appears to increase slightly in the

second experiment, but in fact both values are overpredictions of the true critical Deborah number. Very long induction times of greater than 1000 s are common for onset of the elastic instability very close to the critical rotation rate (Jackson *et al.* 1984; Magda & Larson 1988; McKinley *et al.* 1991*a*). However, to perform such experiments requires careful isolation of the apparatus from external perturbations, and effects such as viscous heating in the fluid, or long term temperature fluctuations in the laboratory. In our experiments we have limited observation times at each rotation rate to about 300 s and after a given De_0 was determined to be stable for this period of time, the motor speed was increased in steps of $\delta\Omega = 0.52$ rad s^{-1}, which corresponds to finite increments in De_0 of 0.42 and 0.65 for the $\beta = 0.59$ and $\beta = 0.84$ fluids, respectively.

The predicted onset radius for the $\beta = 0.59$ fluid at $De_0 = 6.0$ is $R_1^* = 2.2$, which is in good agreement with the experimental results. The value of R_1^* is defined as the radius at which the instability begins to grow; however, because only cells that have already grown to a finite amplitude large enough to produce a discernible peak in the radial intensity profiles (see figure 8) can be detected, the values of R_1^* in table 2 will necessarily tend to overpredict the true onset radius.

The most important difference between the experimental results and the predictions of Öztekin & Brown (1993) is that the Oldroyd-B model predicts that the flow should be unstable for all dimensionless radii greater than R_1^*, whereas there is an experimentally observed position R_2^* beyond which the flow remains stable. Although the critical radius R_1^* for onset of the instability is predicted well for $De_0 = 6$, the analysis using the Oldroyd-B model predicts that the critical radius increases monotonically as the rotation rate is decreased. There should therefore be a larger value of R^* at which secondary flow is observed experimentally for Deborah numbers smaller than $De_0 = 6$. As long as the value of the critical dimensionless radius R_1^* is less than the finite aspect ratio R/H of the experimental apparatus, the instability should be observed from R_1^* outwards to the edge of the disk, and as De_0 is increased, the annular region of unsteady flow should move inwards. For example, for $De_0 \sim 1$, the analysis for the Oldroyd-B model with $\beta = 0.59$ predicts that the flow will be unstable with $m = 3$ at $R_1^* = 19$, whereas for $De_0 \sim 3$, $m = 1$ is the most unstable mode for all dimensionless radii $R^* \geqslant 2.2$. In contrast, experiments show that the flow remains stable at all radii across the disk for all rotation rates below the critical rotation rate corresponding to $De_0 = 6.35$, when the cells form between R_1^* and R_2^*. As shown in §4, this qualitative inconsistency with the linear analysis can be alleviated by considering a more realistic constitutive equation that includes shear-thinning of the first normal stress coefficient.

Furthermore, the linear stability analysis predicts that multiple spiral modes should be present in the secondary flow, whereas it is clear from our observations that only a single mode is observed at short times. For $De(\dot{\gamma}) = 3$, the $m = 1$ mode is predicted to be the most unstable in the sense that it has the smallest critical radius of $R_1^* = 2.2$. However, the modes with $m = 0$ and $m = 2$ are both unstable at the slightly larger radius of $R_1^* = 2.7$. The neutral stability curves yield no information about the temporal growth rates of the different modes, or the amplitudes of the disturbances, and therefore no means of determining which mode should be selected in an experiment.

For the $\beta = 0.84$ fluid, the onset of the instability was again observed at $De_0 \approx 6$ for both aspect ratios, and the shear-rate-dependent Deborah number based on the shear rate at R_1^* was $De(\dot{\gamma}) \approx 3$, as observed for the $\beta = 0.59$ fluid. The analysis for the Oldroyd-B model predicts that for a given De_0, the critical radius R_1^* should be greater for the $\beta = 0.84$ fluid, whereas the observed value of R_1^* is slightly smaller for the $\beta =$

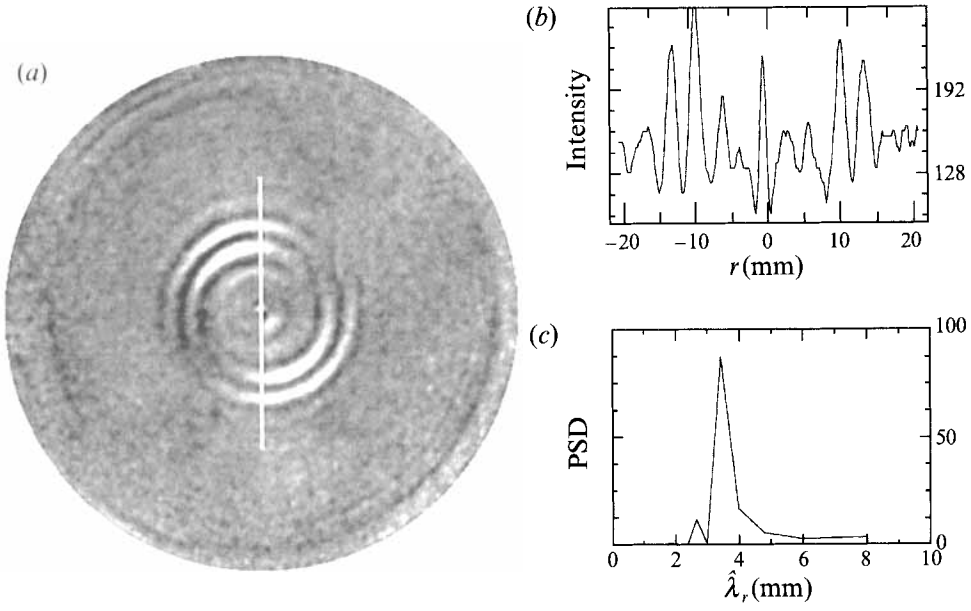

FIGURE 11. Secondary flow (*a*) for a fluid with viscosity ratio $\beta = 0.84$ and aspect ratio $R/H = 20$ at flow conditions $De_0 = 5.85$ and $Re = 0.007$ shows two nested spiral vortices, $m = 2$. Calculation of the wavelength of the disturbance along the line $\theta = +1.57$ rad (*b–c*) gives $\hat{\lambda}_r = 3.41 \pm 0.29$ mm.

0.84 fluid than for the $\beta = 0.59$ fluid. The instability again extended across only a portion of the disk, and R_2^* was found to decrease for the $\beta = 0.84$ fluid.

The secondary flow for the $\beta = 0.84$ fluid between parallel plates with an aspect ratio of $R/H = 20$ was observed to have the form of two nested non-intersecting spirals, as shown in figure 11, whereas for $R/H = 11.4$ a secondary flow with $m = 1$ was observed. Öztekin & Brown predict that the axisymmetric mode should be the most unstable for $\beta = 0.84$ and $De_0 = 6$, although $m = 1$ and $m = 2$ are the next most unstable modes. The wavenumber and wavespeed both scale with the gap size, with the wavenumber increasing and the wavespeed decreasing relative to the $\beta = 0.59$ fluid.

3.4. *Onset of nonlinear interactions*

The results presented in §§ 3.2 and 3.3 are for times shortly after the onset of the instability when the secondary flow consists only of a single spiral vortex which intensifies as it travels across the disks. At longer times, the temporal measurements of normal force shown in figure 4, and the video-images of the spatial form of the secondary flow shown in figure 5 indicate that the subcritical instability eventually saturates as slower growing modes become increasingly important and the flow enters a complex aperiodic state far from the base torsional flow. The beginnings of this transition can be seen in figure 12, which shows results from the experiments with $\beta = 0.84$ and $R/H = 11.4$. The critical De_0 was exceeded at $\hat{t} = 16{:}00$ min, and figures 12(*a–c*) show that initially a single spiral with $m = 1$ and $\hat{\lambda}_r = 5.27$ mm is present which intensifies with time and travels radially outwards across the entire disk. However, at longer times this single spiral begins to split at intermediate radial positions, as shown in figures 12 (*d–f*). A single well-defined spatial wavelength is still discernible, but it is now much shorter than the single mode spiral structures present in the linearly unstable regime, and the characteristic wavenumber has approximately doubled to $\alpha = 6.49$. The primary mode is clearly still in evidence at other radial locations. Similar nonlinear

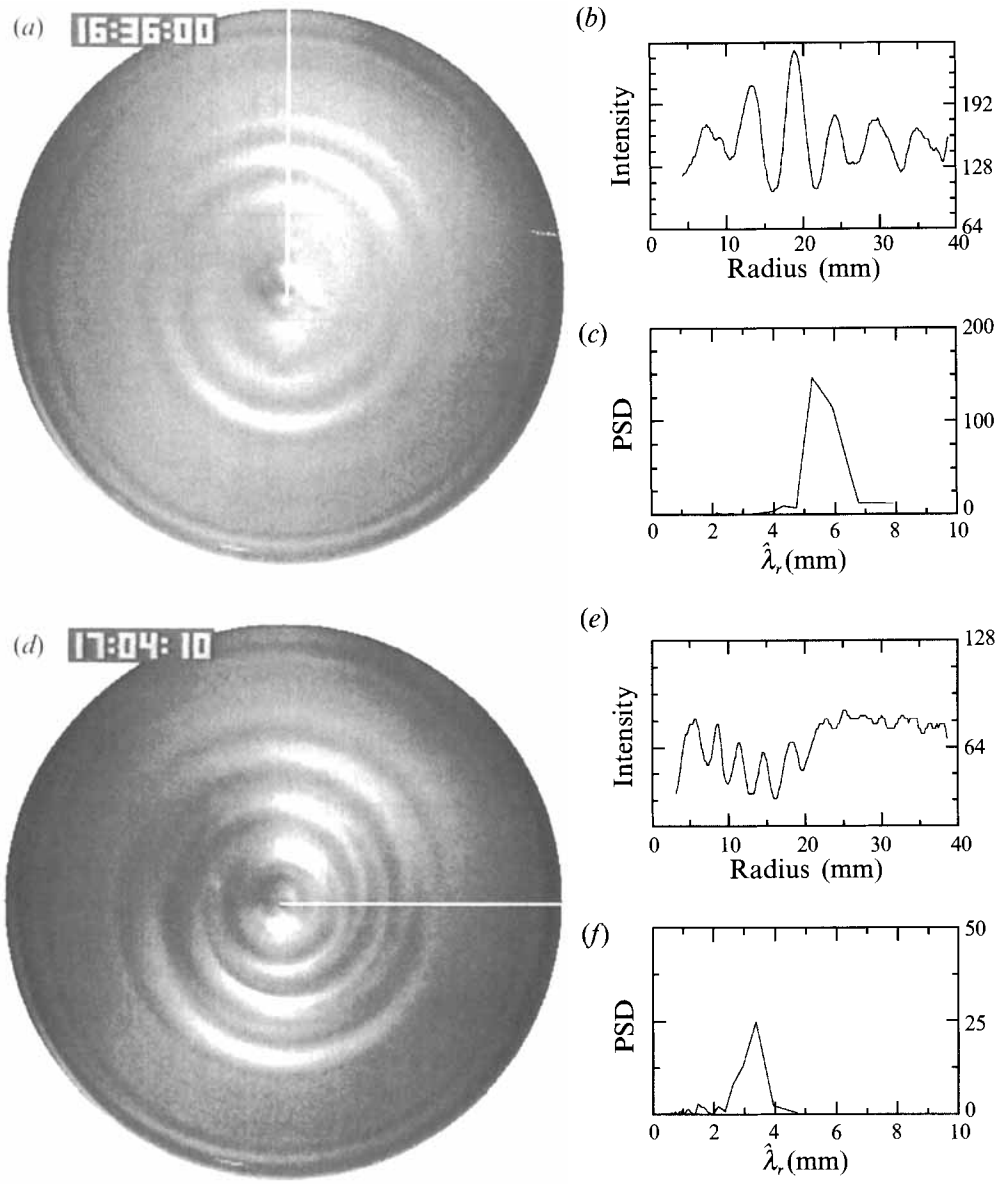

FIGURE 12. Transition to nonlinear state for $\beta = 0.84$ and $R/H = 11.4$ at flow condition $De_0 = 6.18$ and $Re = 0.009$: (*a–c*) initial secondary flow has the form of a single spiral vortex with radial wavelength $\hat{\lambda}_r = 5.27$ mm; (*d–f*) as the instability saturates, the cellular structure splits and the wavelength reduces to $\hat{\lambda}_r = 3.39$ mm.

mode interactions are observed for both fluids and all aspect ratios examined. An example of the final unsteady flow reached at long times is shown in figure 13, for the $\beta = 0.59$ fluid and $R/H = 11.4$. The initial spiral mode was axisymmetric with $m = 0$ and a single well-defined radial wavelength of $\hat{\lambda}_r = 5.94$ mm, and the steady torsional base flow remained stable for all radii less than $\hat{r} = 14.7$ mm. As the Fourier spectrum in figure 13(*c*) shows, the secondary flow can no longer be characterized by a single wavelength. Although considerable power remains in disturbances with wavelengths close to $\hat{\lambda}_r = 6$ mm, shorter wavelength modes also are present. Close examination of

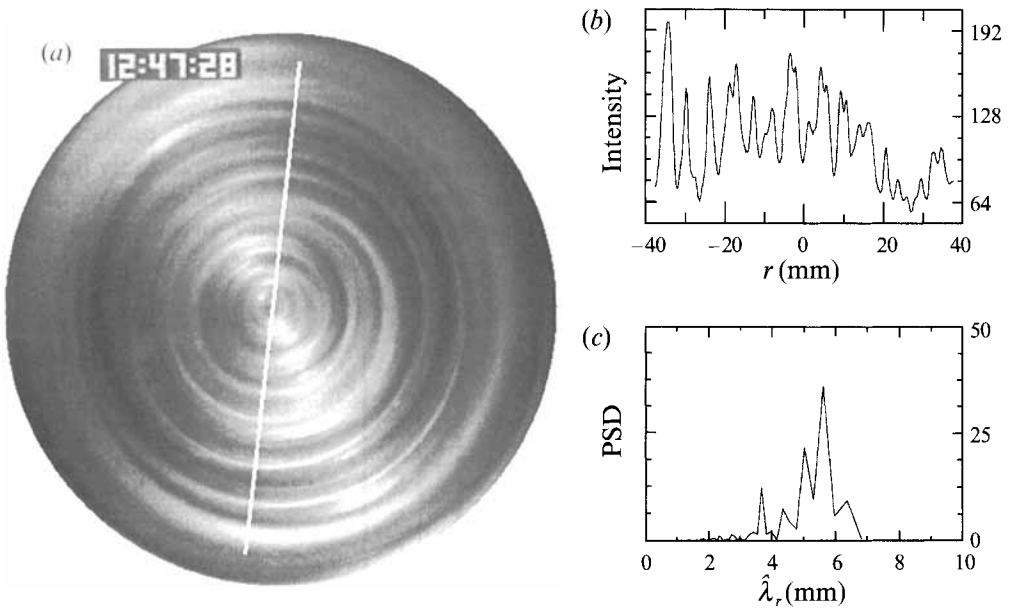

FIGURE 13. Fully nonlinear flow state for $\beta = 0.59$ and $R/H = 11.4$ with multiple modes and wavelengths present after 48 s shearing at $De_0 = 6.35$ and $Re = 0.075$. At short times the flow exhibited a single axisymmetric disturbance with $m = 0$ and $\hat{\lambda}_r = 5.94$ mm.

the videotape and images such as figure 13(*a*) reveal the presence of both positive angle ($m > 0$) and negative angle ($m < 0$) spirals with a wide range of radial wavelengths. These negative angle spirals have negative wavespeeds and move radially inward until the nonlinear time-dependent secondary flow extends across the entire disk.

4. Linear stability analysis

We consider a viscoelastic fluid contained between two parallel coaxial infinite disks separated by a distance H. The flow is driven by the rotation of the bottom plate and is described in the cylindrical coordinate system $(\hat{r}, \theta, \hat{z})$ with $\hat{z} = 0$ positioned on the rotating disk (see figure 1). With inertial effects neglected by setting the Reynolds number to zero, the equations governing mass and momentum conservation are $\boldsymbol{\nabla} \cdot \hat{\boldsymbol{u}} = 0$ and $\boldsymbol{\nabla} \cdot \hat{\boldsymbol{\tau}} - \boldsymbol{\nabla}\hat{p} = \mathbf{0}$, where $\hat{\boldsymbol{u}}$ is the velocity vector, $\hat{\boldsymbol{\tau}}$ is the extra stress tensor, and $\hat{p}$ is the pressure. The polymeric contribution to the extra stress tensor is given by (6) and the total extra stress tensor $\hat{\boldsymbol{\tau}}$ is decomposed as $\hat{\boldsymbol{\tau}} \equiv \hat{\boldsymbol{S}} + \eta_s \dot{\boldsymbol{\gamma}}$, where $\dot{\boldsymbol{\gamma}} \equiv (\boldsymbol{\nabla}\hat{\boldsymbol{u}})^T + \boldsymbol{\nabla}\hat{\boldsymbol{u}}$ is the dimensional rate-of-strain tensor and η_s is the solvent viscosity. The no-slip and no-penetration boundary conditions on the velocity field at the upper and lower plates are: $\hat{\boldsymbol{u}}^T = (0, \hat{r}\Omega, 0)$ at $\hat{z} = 0$ and $\hat{\boldsymbol{u}}^T = (0, 0, 0)$ at $\hat{z} = H$. The velocity field describing the steady-state viscometric flow is given by $\hat{\boldsymbol{u}}_0^T = [0, \Omega\hat{r}(1 - \hat{z}/H), 0]$. As discussed above, the Chilcott–Rallison constitutive equation is used to describe the Boger fluids used in the experiments. For the Chilcott–Rallison model the corresponding stress and pressure field, $\hat{\boldsymbol{S}} = \hat{\boldsymbol{S}}_0$ and $\hat{p} = \hat{p}_0$, are given in component form as $\hat{S}_{0rr} = \hat{S}_{0r\theta} = \hat{S}_{0rz} = \hat{S}_{0zz} = 0$; $\hat{S}_{0\theta z} = -\eta_p \Omega\hat{r}/H$. The value of the hoop stress $\hat{S}_{0\theta\theta}$ is given by

$$\hat{S}_{0\theta\theta} = \frac{\eta_p L^2}{2\lambda_1}[-1 + (1 + 8(\lambda_1 \Omega)^2(\hat{r}/H)^2(L^2 - 3)/L^4)^{\frac{1}{2}}], \tag{7}$$

and the pressure is computed as $\hat{p}_0 \equiv \int(\hat{S}_{0\theta\theta}/\hat{r})\,\mathrm{d}r$.

The linear stability analysis for the Chilcott–Rallison model is similar to the presentation by Öztekin & Brown (1993). Equations governing the evolution of small normal mode disturbances applied to the viscometric base flow are formed for dimensionless variables scaled with $(H,\ \Omega^{-1},\ H\Omega,\ \eta_0\Omega)$ for (length, time, velocity, stress), respectively. We restrict the analysis to disturbances that are radially localized in r. The spatial dependence of each disturbance equation can be separated, if the disturbance is written in the Fourier form of (1) and the velocity, pressure, and stress fields are given as

$$\begin{bmatrix} \tilde{u}_r \\ \tilde{u}_\theta \\ \tilde{u}_z \\ \tilde{p} \\ \tilde{S}_{rr} \\ \tilde{S}_{r\theta} \\ \tilde{S}_{rz} \\ \tilde{S}_{\theta\theta} \\ \tilde{S}_{\theta z} \\ \tilde{S}_{zz} \end{bmatrix}(r,\theta,z,t) = \begin{bmatrix} 0 \\ r(1-z) \\ 0 \\ p_0 \\ 0 \\ 0 \\ 0 \\ S_{0\theta\theta} \\ S_{0\theta z} \\ 0 \end{bmatrix} + \begin{bmatrix} U \\ V \\ W \\ p \\ S_{rr} \\ S_{r\theta} \\ S_{rz} \\ S_{\theta\theta} \\ S_{\theta z} \\ S_{zz} \end{bmatrix} e^{i\alpha r + im\theta + \sigma t}, \tag{8}$$

where $S_{0\theta z} \equiv -\beta_p r, S_{0\theta\theta} \equiv \hat{S}_{0\theta\theta}/(\eta_0\Omega), p_0 \equiv \hat{p}_0/(\eta_0\Omega), \beta \equiv \eta_s/\eta_0, \beta_p \equiv (1-\beta), (\tilde{u}_r, \tilde{u}_\theta, \tilde{u}_z)$ are the dimensionless (radial, azimuthal, axial) components of the velocity field, $\tilde{p}$ is the pressure, $(\tilde{S}_{rr}, \tilde{S}_{r\theta}, \tilde{S}_{rz}, \tilde{S}_{\theta\theta}, \tilde{S}_{\theta z}, \tilde{S}_{zz})$ are the components of the contribution to the polymeric stress tensor, (U, V, W) are the components of the amplitude of the disturbance to the velocity field, p is the amplitude of the disturbance to the pressure, and $(S_{rr}, S_{r\theta}, S_{rz}, S_{\theta\theta}, S_{\theta z}, S_{zz})$ are the amplitudes of the disturbances to the polymer contribution to the extra stress. As discussed above, the Deborah number is defined in terms of the time constant λ_1 as $De_0 \equiv \lambda_1\Omega$. Here α is the dimensionless radial wavenumber of the disturbance, m is an integer (which can be positive, zero, or negative), and σ is the dimensionless temporal eigenvalue (which can be complex). Substituting (8) into the momentum conservation and constitutive equations and subsequently eliminating the pressure using the continuity equation yields

$$\left[-\mathrm{D}^4+\left(2\kappa^2-\frac{1}{R^{*2}}\right)\mathrm{D}^2-\kappa^4\right]W+\frac{2\beta\xi m}{R^{*2}}\mathrm{D}V-\frac{2\beta m^2}{R^{*3}}\mathrm{D}U-\xi^2\mathrm{D}S_{rr}+\frac{m(-2\xi+1/R^*)}{R^*}\mathrm{D}S_{r\theta}$$

$$+i\xi(\mathrm{D}^2+\kappa^2)S_{rz}-\frac{(i\xi-m^2/R^*)}{R^*}\mathrm{D}S_{\theta\theta}+\frac{im(\mathrm{D}^2+\kappa^2)}{R^*}S_{\theta z}+\mathrm{D}S_{zz}=0, \tag{9a}$$

$$(\mathrm{D}^2-\kappa^2-1/R^{*2})\omega+\frac{2\beta m^2}{R^{*3}}V+\frac{2\alpha\beta m}{R^{*2}}U-\alpha\xi S_{rr}+(-m^2+\alpha\xi-i\alpha/R^*)S_{r\theta}$$

$$+\frac{im}{R^*}\mathrm{D}S_{rz}-\frac{m(-i/R^*+\alpha)}{R^*}S_{\theta\theta}-i\alpha\mathrm{D}S_{\theta z}+\mathrm{D}S_{zz}=0, \tag{9b}$$

where $\xi \equiv \alpha - i/R^*$ and $\kappa^2 \equiv -\alpha\xi - m^2/R^{*2}$. Here $\mathrm{D} \equiv \mathrm{d}/\mathrm{d}z$ and $\omega(z) \equiv i\alpha V(z) - imU(z)/R^* \equiv \varpi(z) - V(z)/R^*$, where $\varpi(z)$ is the amplitude of the disturbances to the vertical vorticity and $\omega(z)$ approximates the amplitude of the disturbance to the vertical vorticity for large values of R^*. In this form $R^* \equiv \hat{r}^*/H$ is the dimensionless radial

location for the localized disturbance. The linearized components of the constitutive equations are

$$P_1 S_{rr} - 2i\alpha\beta U = 0, \tag{10a}$$

$$P_1 S_{r\theta} + DeR^* S_{rz} + \beta_p(-2i\alpha\beta_p DeR^* - 2im/R^* + DeR^* D) U + \beta_p(1/R^* - i\alpha) V = 0, \tag{10b}$$

$$P_1 S_{rz} + \beta_p(imDe - D) U - i\alpha\beta_p W = 0, \tag{10c}$$

$$P_1 S_{\theta\theta} + (P_2 + 2DeR^* S_{0\theta z}\delta_3)(S_{rr} + S_{\theta\theta} + S_{zz}) + 2DeR^* S_{\theta z} + \left(\frac{\beta_p}{R^*} + \frac{De}{f_0}\frac{dS_{0\theta\theta}}{dr}\right) U + \beta_p(-4imDe^2 R^* - 2im/R^* + 2DeR^* D) V = 0, \tag{10d}$$

$$P_1 S_{\theta z} + P_2(S_{rr} + S_{\theta\theta} + S_{zz}) + DeR^* S_{zz} + \beta_p(-imDe - D) V - \frac{De}{f_0}\frac{dS_{0\theta z}}{dr} U + \beta_p(-2imDe^2 R^* - im/R^* - DeR^* D) W = 0, \tag{10e}$$

$$P_1 S_{zz} + \beta_p(2imDe - 2D) W = 0, \tag{10f}$$

where $De \equiv De_0/f_0$, $P_1 \equiv [1 + De\sigma + imDe(1-z)]$, $P_2 \equiv -De\delta_1(\sigma + im/R^*) S_{0\theta\theta}/f_0$, $f_0 \equiv \delta_1 + \delta_2 S_{0\theta\theta}$ is the basic state value of the spring nonlinearity f in the Chilcott–Rallison model with $\delta_1 \equiv L^2/(L^2-3)$, $\delta_2 \equiv De_0/[\beta_p(L^2-3)]$ and $\delta_3 \equiv -De_0^2(L^2-3)/[\beta_p(L^2 + De_0 S_{0\theta\theta})^2]$. It is worth noting in (10*b*)–(10*f*) that the finite extensibility of the dumb-bells in the shear flow implied by $f_0 > 1$ serves to reduce the apparent Deborah number defined by $De \equiv De_0/f_0$ that appears in the disturbance equations. We expect shear-thinning in the first normal stress coefficient to increase the critical value of the zero-shear-rate Deborah number for the onset of instability. The boundary conditions on the disturbance velocities are

$$W(0) = DW(0) = \omega(0) = W(1) = DW(1) = \omega(1) = 0. \tag{11a–f}$$

The solution method involves approximation of the eigenvalue problem by the mixed Galerkin–Tau/Chebyshev method and numerical solution of the resulting generalized eigenvalue problem; details are given in the Appendix.

The stability of the viscometric flow is characterized for given values of De_0 and m by neutral stability curves $R^* = R^*(\alpha)$ along which $Re(\alpha) = 0$. These curves are determined by computing the growth rate σ for fixed values of (α, m, De_0, L) and several values of R^* and using bisection to determine the critical value $R^*(\alpha)$. These searches are carried out to one part in 10^6.

4.1. *Results of the linear stability analysis*

The effects of shear-thinning on the onset of elastic instabilities for the viscoelastic flow between rotating infinite disks were explored by calculations for the axisymmetric mode ($m = 0$) and positive angle spirals ($m > 0$) for two specific solvent viscosity ratios of $\beta = 0.59$ and 0.84 and for representative values of viscosity ratio in the range of $0.30 \leqslant \beta \leqslant 0.90$. The stability results are presented for Deborah numbers and extensibilities in the range $0 \leqslant De_0 \leqslant 8$ and $10 \leqslant L < \infty$, respectively.

The calculations were first verified by comparing the results for $L = 1000$ with the earlier calculations by Öztekin & Brown (1993) for viscoelastic flow modelled by the Oldroyd-B constitutive equation ($L \to \infty$) between parallel rotating disks. The neutral stability curves $R^* = R^*(\alpha)$, the critical onset radius and radial wavenumber for positive and negative angle spirals differ by less than one part in 50, hence we only present stability results for positive angle spirals. As was the case for the Oldroyd-B

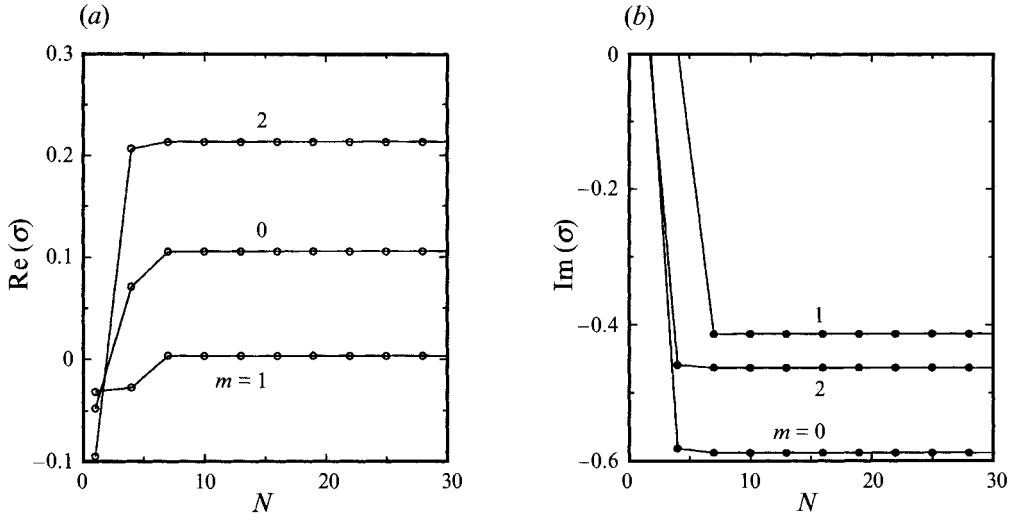

FIGURE 14. (*a*) The real and (*b*) the imaginary parts of the least stable axisymmetric ($m = 0$) and $m = 1$ and $m = 2$ non-axisymmetric eigenvalues as functions of the number of polynomials N in the expansion for $De_0 = 2$ and for $R^* = 10$, $\beta = 0.59$, $L = 50$ and $\alpha = 3$.

model (Öztekin & Brown 1993), the only significant difference between positive and negative angle spirals is found in the wave speed: positive angle spirals travel radially outward, whereas negative angle spirals travel radially inward.

The accuracy of the mixed Galerkin–Tau/Chebyshev approximation for the eigenvalue problem was tested by checking the spectral convergence of the eigenvalues with the smallest real part. The real and imaginary parts of the least stable axisymmetric ($m = 0$) and non-axisymmetric ($m = 1$ and $m = 2$) eigenvalues are plotted in figure 14 as a function of the number of polynomials in the expansions shown in (A 1) in the Appendix for $De_0 = 2$ and $L = 50$ and for the parameter value $R^* = 10$, $\beta = 0.59$, and $\alpha = 3$. For each value of m, both the real and imaginary parts of the eigenvalue converge for values of N as small as ten. With this method, the spectral convergence rate of non-axisymmetric modes is dramatically increased compared to the Galerkin/Chebyshev approximation used by Öztekin & Brown (1993).

The neutral stability curves $R^* = R^*(\alpha)$ computed for axisymmetric ($m = 0$) and non-axisymmetric ($m = 1$) disturbances for $\beta = 0.59$ and several values of the dumbbell extensibility L are shown in figure 15 for $De_0 = 1$ and $De_0 = 5$. The solid curve in each plot represents the neutral stability curve $R^* = R^*(\alpha)$ for the Oldroyd-B limit, $L \to \infty$. For the Oldroyd-B model, there is a critical value $R^* = R^*_{crit}(\alpha_{crit})$ at each Deborah number that corresponds to the minimum in the neutral stability curve $R^* = R^*(\alpha)$. For $R^* < R^*_{crit}(\alpha_{crit})$ the viscometric flow is stable for all values of the radial wavenumber α, whereas for any $R^* > R^*_{crit}(\alpha_{crit})$ the flow is unstable to disturbances in some range of α, as previously shown by Öztekin & Brown (1993). The shape of the neutral stability curves for the nonlinear Chilcott–Rallison model is fundamentally different. These neutral stability curves form closed loops; as a result, there is a finite range of radii $R^*_{1crit}(\alpha_{1crit}) < R^* < R^*_{2crit}(\alpha_{2crit})$ for which the viscometric base flow is unstable. For all radii outside this range, i.e. $R^* < R^*_{1crit}(\alpha_{1crit})$ and $R^* > R^*_{2crit}(\alpha_{2crit})$, the steady flow is stable. The values R^*_{1crit} and R^*_{2crit} are, respectively, the minimum and maximum of the neutral stability curves $R^* = R^*(\alpha)$. As L decreases and shear-thinning of $\Psi_1(\dot{\gamma})$ becomes increasingly important, the unstable region

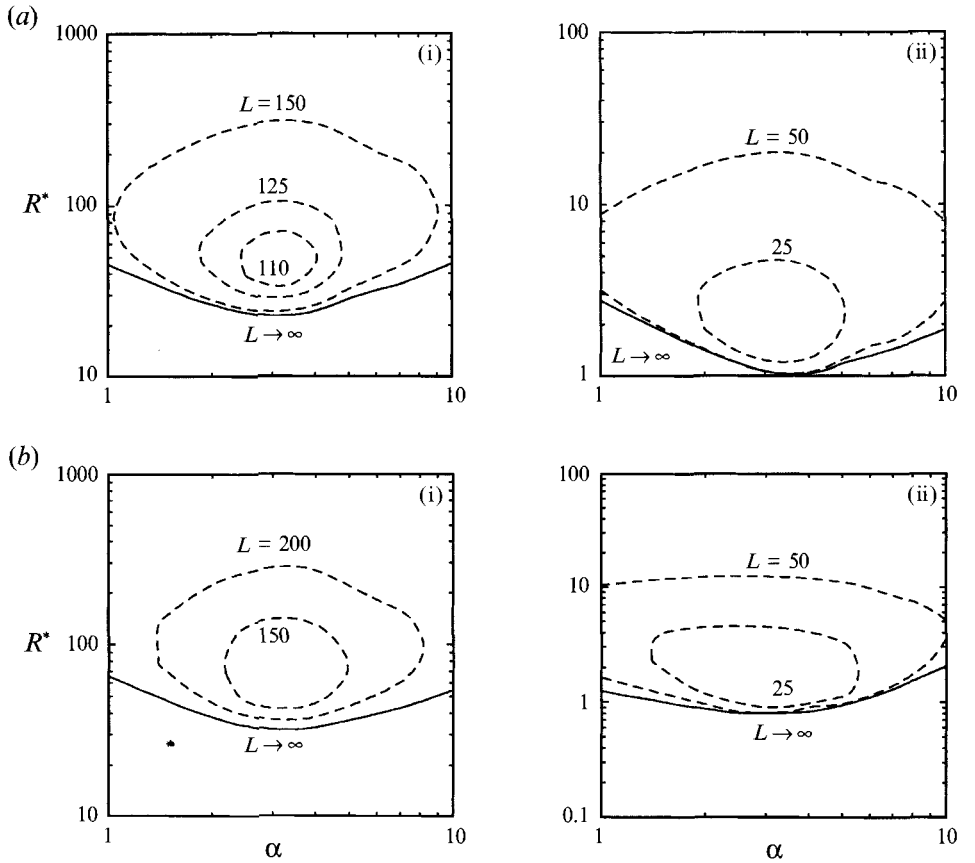

FIGURE 15. The neutral stability curves $R^* = R(\alpha, m)$ computed for the Chilcott–Rallison model with $\beta = 0.59$ and various values of L for (*a*) axisymmetric ($m = 0$) and (*b*) $m = 1$ non-axisymmetric disturbances with Deborah numbers of (i) $De_0 = 1$ and (ii) $De_0 = 5$.

contained by R^* becomes smaller and ultimately disappears completely below a critical value of L. Monotonically increasing De_0 reduces the critical radii $R^* = R^*_{crit}(\alpha_{crit})$ for all curves, but also decreases the critical value of the extensibility L for which the flow is stable everywhere to both axisymmetric and non-axisymmetric disturbances. The critical value of the radial wavenumber changes little with De_0. The most dangerous radial wavenumbers for the onset ($\alpha_{1\,crit}$) and for disappearance ($\alpha_{2\,crit}$) of the instability remain close to about $\alpha \approx 3$ for both axisymmetric and non-axisymmetric disturbances; this wavenumber corresponds to disturbances with a wavelength of approximately twice the gap spacing.

Finite extensibility has only a small stabilizing effect on the value of $R^*_{1\,crit}$ compared to the value obtained for the Oldroyd-B model. For low shear rates, the Chilcott–Rallison model predicts quadratic growth in the basic state values of hoop stress $\hat{S}_{0\theta\theta}$; see (7). However, for dimensionless shear rates exceeding $De_0 R^* \geqslant L^2/(8(L^2-3))^{\frac{1}{2}}$ shear-thinning in the normal stress becomes appreciable and the neutral curves in figure 15 deviate significantly from the Oldroyd-B limit. Ultimately, for $R^* > R^*_{2\,crit}(\alpha_{2\,crit})$ the shear-thinning reduces the gradient in the normal stress to the extent that the steady viscometric motion is restabilized.

Contours of the eigenfunction corresponding to the disturbance in the axial velocity in the (r, z)-plane between the plates are shown in figure 16 for one radial wavelength

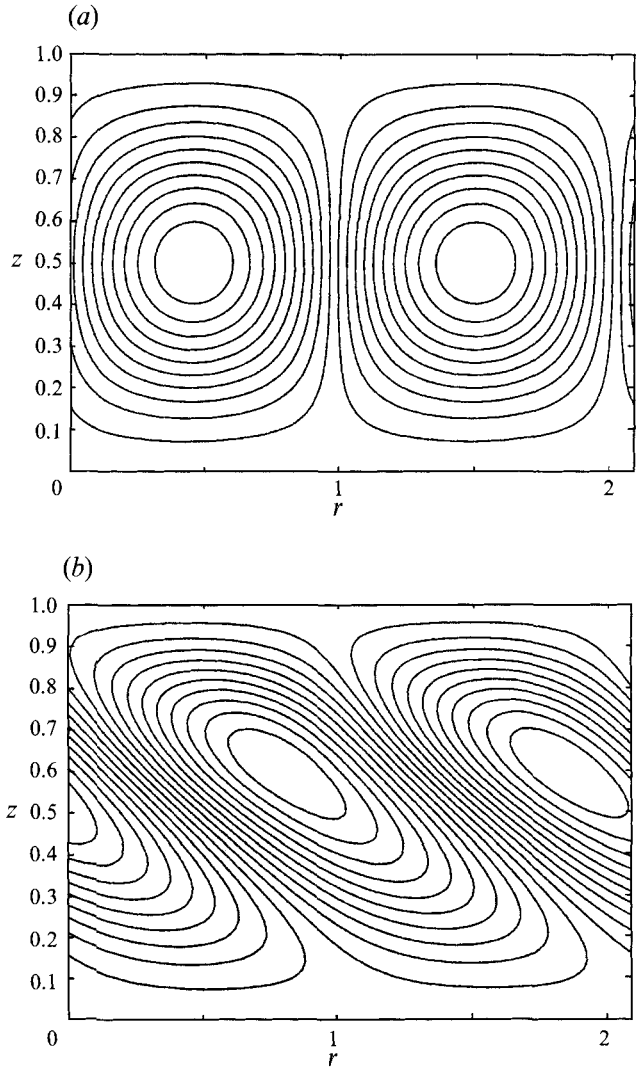

FIGURE 16. Contours of the vertical velocity $\tilde{u}_z$ of the disturbance calculated for the Chilcott–Rallison model ($\beta = 0.59$, $L = 50$) in the (r, z)-plane. Plots are for (*a*) the axisymmetric disturbances ($m = 0$), $De_0 = 2$, $R^* = 5.85$ and $\alpha = 3$ and (*b*) $m = 1$ non-axisymmetric disturbances, $De_0 = 2$, $R^* = 9.2$ and $\alpha = 3$.

of the axisymmetric ($m = 0$) and non-axisymmetric ($m = 1$) disturbance flows, as computed for the critical values $R^* = R^*_{1crit}(\alpha_{1crit})$ with $De_0 = 2$, $L = 50$ and $\beta = 0.59$. The vertical velocity of the axisymmetric disturbances is symmetric about the midplane ($z = 0.5$), has a maximum amplitude at the midplane and is zero at each disk ($z = 0$, $z = 1$). The non-axisymmetric velocity eigenfunction is not symmetric about the midplane, but is skewed in the radial direction and has maximum intensity closer to the stationary disks. Although, it is not plotted here, the axial eigenfunction for the $m = -1$ non-axisymmetric mode is skewed in the opposite radial direction to the eigenfunction for the positive angle spirals. These eigenfunctions have very similar forms to those computed by Öztekin & Brown (1993) for the Oldroyd-B constitutive model.

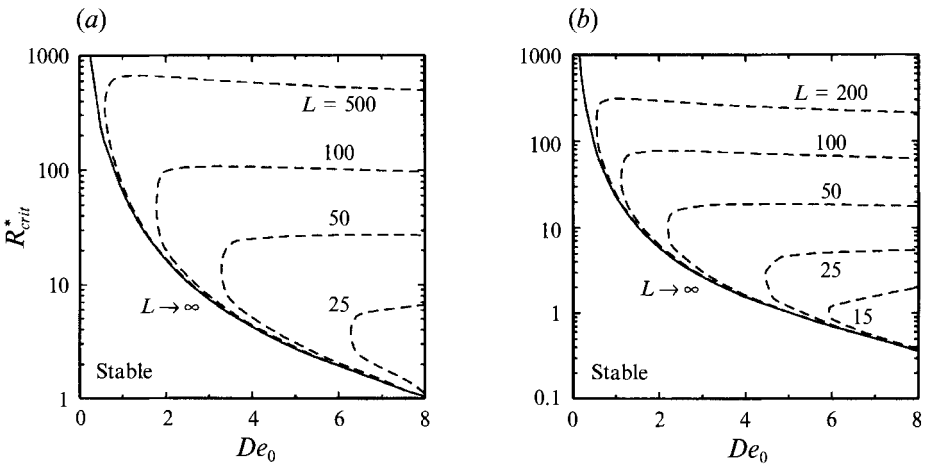

FIGURE 17. The critical radius R^*_{crit} for the onset of the axisymmetric instability as a function of De_0 for a viscosity ratio of (*a*) $\beta = 0.90$ and (*b*) $\beta = 0.59$.

The travelling-wave form of the disturbance and the shape of the neutral stability curves gives a picture of the instability that is consistent with our experimental observations. For a parallel plate apparatus with given aspect ratio, R/H, the instability is expected to start when the Deborah number is increased beyond a finite critical value that depends on the rheology of the fluid (given by the parameters β and L). For De_0 above this value, travelling spiral vortices are expected to emanate from the critical dimensionless radius $R^* = R^*_{1crit}(\alpha_{1crit})$, move radially outward and diminish beyond a second critical radius $R^* = R^*_{2crit}(\alpha_{2crit})$. The critical value of the radius $R^* = R^*_{crit}(\alpha_{crit})$ for the onset of the axisymmetric instability is plotted in figure 17 for the viscosity ratios of $\beta = 0.59$ and $\beta = 0.90$ and several values of L. In the Oldroyd-B limit, $L \to \infty$, a finite value of the critical onset radius is predicted for any non-zero value of Deborah number. However, for the shear-thinning model (finite values of L) there exists a critical value of Deborah number De_{0crit}, below which the viscometric motion is stable everywhere for all dimensionless radii. The base flow is unstable in the finite range of dimensionless radii $R^*_{1crit}(\alpha_{1crit}) < R^* < R^*_{2crit}(\alpha_{2crit})$ for $De_0 > De_{0crit}$.

For all values of the viscosity ratio β, the value of De_{0crit} increases and the range of radii where the base flow is unstable shrinks as L is decreased and the shear-rate-dependence of the first normal stress coefficient becomes increasingly important. Note also that the predictions of the critical radii for the onset of instability R^*_{1crit} are very similar for both the Oldroyd-B and the Chilcott–Rallison models and that the critical value of R^*_{2crit} predicted by the Chilcott–Rallison fluid for any value of L has a weak dependence on De_0, as shown in figure 17. These features of the neutral stability diagram can be explained better by plots of the apparent Deborah number $De \equiv De_0/f_0$ as a function of dimensionless radius, as shown in figure 18 for $\beta = 0.59$, $1 \leqslant De_0 \leqslant 8$ and $L = 50$. The apparent Deborah number asymptotes to zero for all values of De_0 and any finite value of L owing to shear-thinning in the first normal stress coefficient. For $L = 50$, the difference in the apparent Deborah number for $3 \leqslant De_0 \leqslant 8$ is very small for radii beyond $R^* \approx 20$. This is consistent with the linear stability analysis for this fluid, which predicts the value of $R^*_{2crit}(\alpha_{2crit}) \cong 20$, approximately independent of De_0. However, for much smaller values of R^* the shear-thinning of the normal stress is small and the apparent Deborah number is not reduced significantly below the zero-

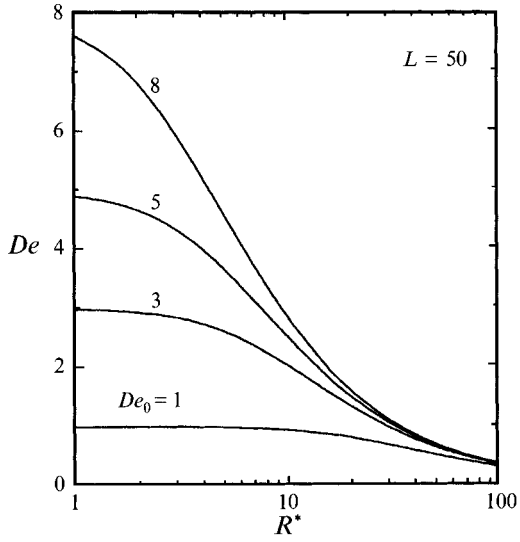

FIGURE 18. The apparent Deborah number, $De \equiv De_0/f_0$, as a function of R^* for a viscosity ratio $\beta = 0.59$, $1 \leqslant De_0 \leqslant 8$ and a dumb-bell extensibility of $L = 50$.

shear value of De_0. Therefore, the differences between the predictions of R^*_{1crit} for the Oldroyd-B and the Chilcott–Rallison models are small; this is seen in figure 17.

The results in figure 17(*b*) show that no instability should be expected below a critical Deborah number $De_0 \approx 6$, for a fluid described by $\beta = 0.59$ and $L \approx 15$. Beyond this rotation rate disturbances are expected to be radially localized to a thin annular ring. This prediction is in good qualitative agreement with the experimental results shown in table 2. A more detailed comparison between our linear stability calculations and observations is discussed in §5.

The critical value of the radius $R^* = R^*_{crit}(\alpha_{crit}; m)$ for $\beta = 0.59$ is plotted in figure 19 for the most dangerous, the axisymmetric ($m = 0$), and the non-axisymmetric modes with $m = 1$ and $m = 2$. The solid curves in each plot denote the critical value of the radius for the most unstable modes in the range of $m \leqslant 10$. For the Oldroyd-B constitutive equation, the axisymmetric disturbance is never the most dangerous; however, the difference in the critical radii between the axisymmetric and the $m = 1$ and $m = 2$ non-axisymmetric modes is small, as shown in figure 19(*a*). The non-axisymmetric modes with $m > 2$ which become most unstable for $De_0 < 2$ are omitted for clarity. For finite values of L, the critical radius R^*_{1crit} for the $m = 1$ mode is always the smallest while the critical radius R^*_{2crit} is largest for the axisymmetric and $m = 2$ modes. The differences in the critical radii are still small for all three modes, indicating that spiral vortices and the axisymmetric instability might all be seen simultaneously in the flow visualization experiments. Similarly, the critical value of the radius $R^* = R^*_{crit}(\alpha_{crit}; m)$ for $\beta = 0.84$ is plotted in figure 20 for the axisymmetric ($m = 0$) and $m = 1$ and $m = 2$ non-axisymmetric modes. In addition to changing the relative ordering of the stability of each mode, note that increasing β results in an overall increase in the stability of the flow; the neutral curves in figure 20 are all shifted to higher values of De_{0crit} for any L. The axisymmetric disturbance is the most dangerous, but the critical radii of all modes are again very similar for all values of L. As was the case for $\beta = 0.59$, the axisymmetric and non-axisymmetric instabilities may be difficult to distinguish in experiments.

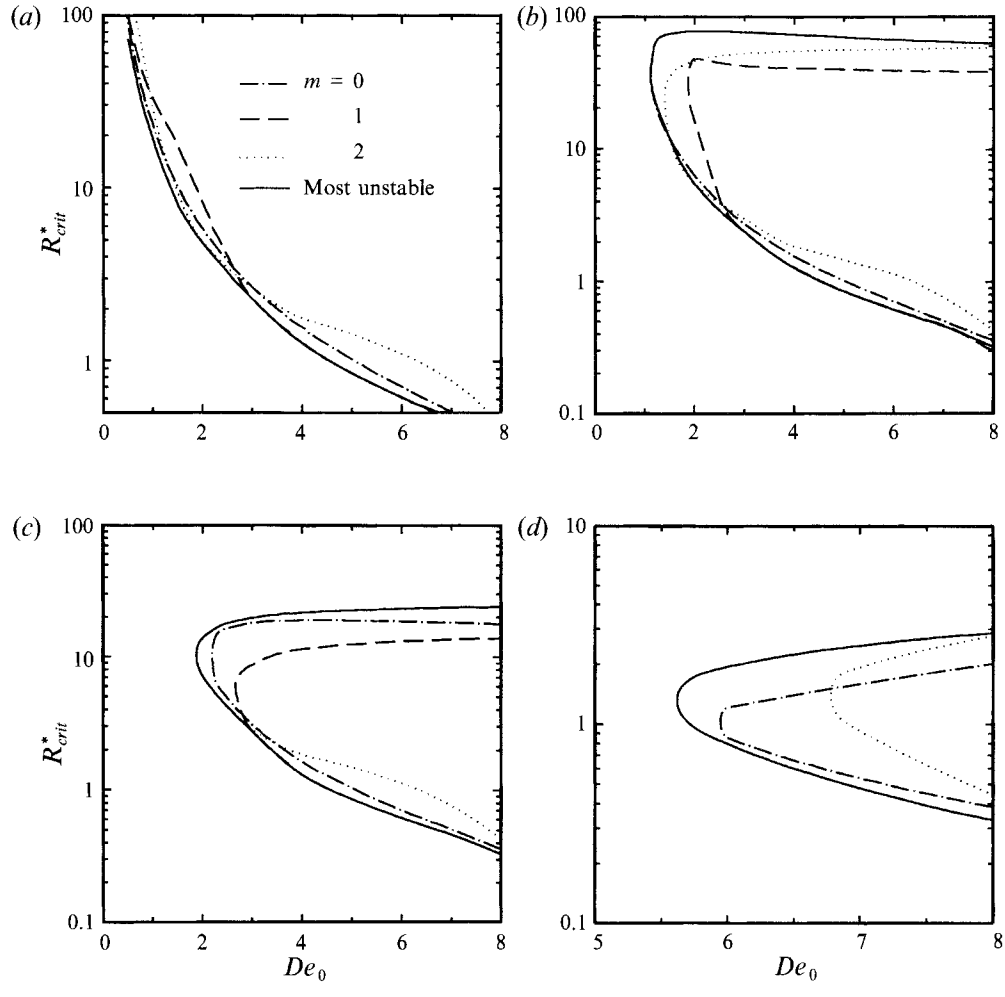

FIGURE 19. The critical radius R^*_{crit} for the onset of the most dangerous, axisymmetric ($m = 0$), and non-axisymmetric ($m = 1$ and $m = 2$) instabilities as a function of De_0 for a viscosity ratio of $\beta = 0.59$ and extensibilities of (*a*) $L \to \infty$, (*b*) $L = 100$, (*c*) $L = 50$ and (*d*) $L = 15$.

4.2. *Disturbance-energy analysis*

The mechanism of the instability in the flow between the parallel rotating disks is most clearly seen from the disturbance-energy equation. The mechanical energy balance of the system is evaluated to determine the energy transfer between the mean flow and the disturbance flow, by a method similar to the one developed by Joo & Shaqfeh (1991, 1992, 1994) for analysing purely elastic instabilities of the Oldroyd-B model in the Taylor–Couette and Taylor–Dean flows.

The energy analysis here is for a modified constitutive equation in which the terms proportional to the material derivation $\mathrm{D}f/\mathrm{D}t$ implicit in (6) are neglected. This model is used by Coates, Armstrong & Brown (1992) to calculate the steady-state viscoelastic flow through an axisymmetric contraction and is referred to as the modified Chilcott–Rallison (MCR) model. The dimensionless form of this constitutive equation is written as

$$\boldsymbol{S} + \frac{De_0}{f}\boldsymbol{S}_{(1)} = (1-\beta)\dot{\gamma}. \tag{12}$$

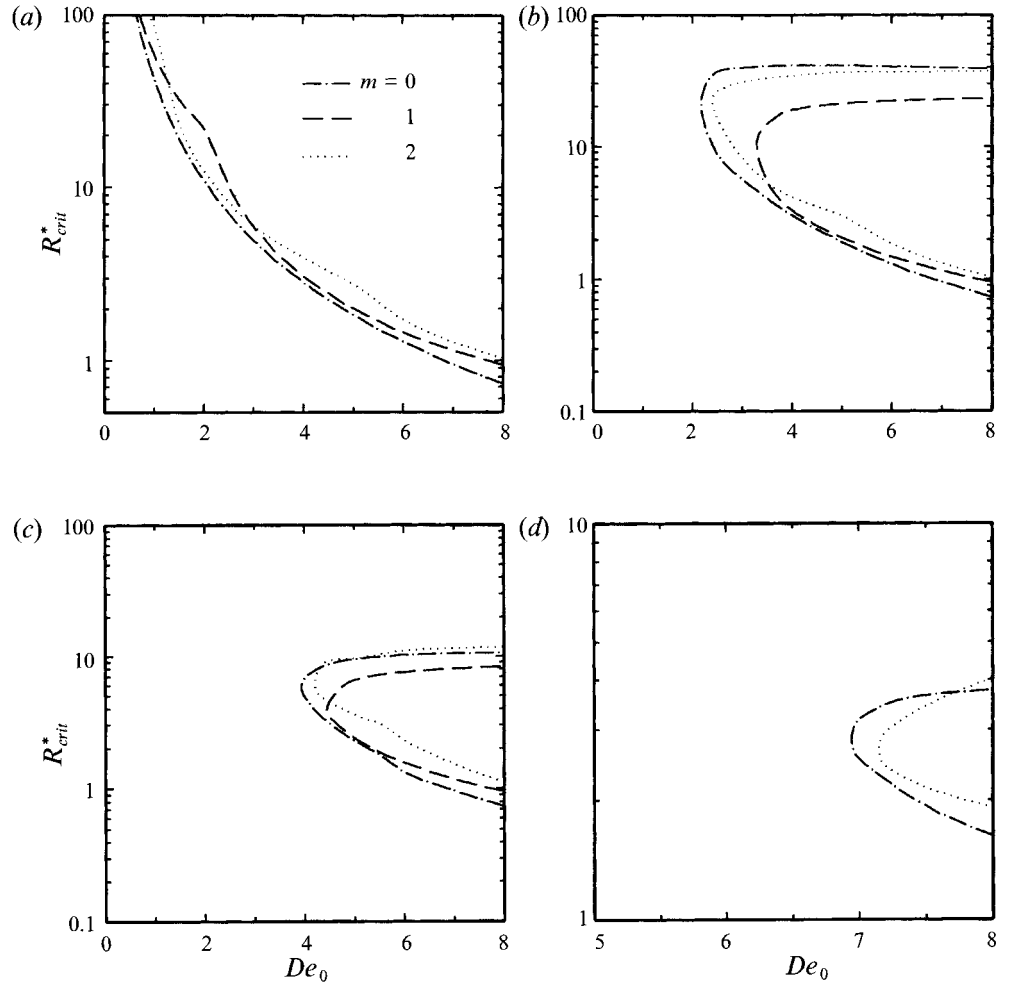

FIGURE 20. The critical radius R^*_{crit} for the onset of the axisymmetric ($m = 0$) and non-axisymmetric ($m = 1$ and $m = 2$) instabilities as a function of De_0 for a viscosity ratio of $\beta = 0.84$ and extensibilities of (*a*) $L \to \infty$, (*b*) $L = 100$, (*c*) $L = 50$ and (*d*) $L = 20$.

This model predicts almost identical rheological response in steady flows to the full Chilcott–Rallison model, and the neglect of the Df/Dt terms allows us to obtain valuable insight into the evolution of the disturbance-energy in the secondary flow through the analytical relations derived below.

The critical value of the radius $R^* = R^*_{crit}(\alpha_{crit})$ for the onset of the instability of the axisymmetric disturbances computed using the full Chilcott–Rallison models (dashed curves) and the modified Chilcott–Rallison model (solid curves) are plotted in figure 21 for $\beta = 0.59$ and for several values of the extensibility parameter L, which controls the shear-thinning in both models. The values of the critical radius R^*_{1crit} and the critical Deborah number De_{0crit} are very similar for both models. The predictions of R^*_{2crit} differ; the extra terms neglected in the MCR constitutive equation further stabilize the base flow when the fluid is highly shear-thinning.

The mechanical energy equation is obtained by multiplying the linearized

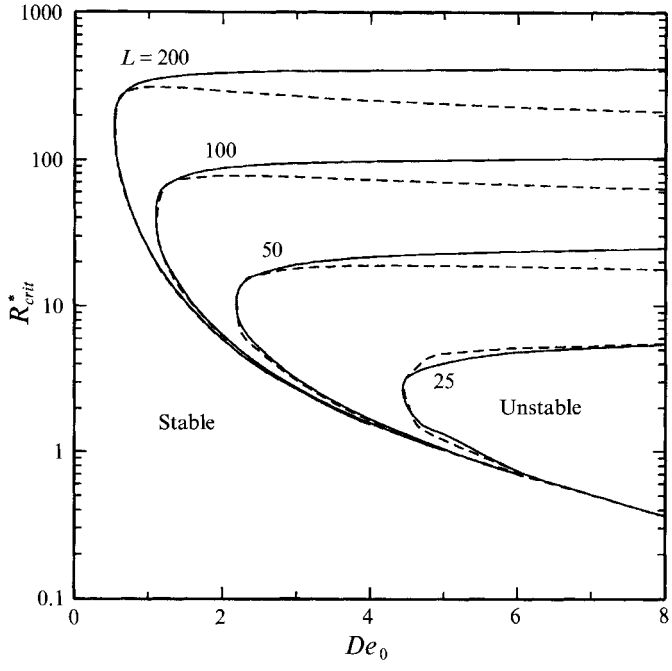

FIGURE 21. The critical dimensionless radius or aspect ratio $R^* = R^*_{crit}(\alpha_{crit})$ for the onset of the axisymmetric instability computed for $\beta = 0.59$ as a function of the Deborah number. ---, Chilcott–Rallison model; ——, modified Chilcott–Rallison model.

disturbance momentum equation by the disturbance velocity and integrating over the periodic volume element $V: 0 < r < 2\pi/\alpha, 0 < \theta < 2\pi/m, 0 < z < 1$. The result is

$$\frac{\mathrm{d}\epsilon_p}{\mathrm{d}t} = Q_{vis} + Q_{pv} + Q_{ps} + Q_{st}, \tag{13}$$

where ϵ_p is the total rate of energy created or dissipated by the disturbance polymeric stresses, and is written as

$$\epsilon_p = \tfrac{1}{2} De \int (\nabla \cdot \boldsymbol{S}) \cdot \boldsymbol{u} \, \mathrm{d}V. \tag{14a}$$

The individual contributions to (13) are identified as follows. The term

$$Q_{vis} = \int (\nabla^2 \boldsymbol{u}) \cdot \boldsymbol{u} \, \mathrm{d}V \tag{14b}$$

is the rate of viscous energy dissipation by the disturbance flow. The term Q_{pv} is the rate of energy production due to the coupling between the base state polymeric stresses and the disturbance velocity field and is written as

$$Q_{pv} = De_0 \int \nabla \cdot \frac{1}{f_0} (-\boldsymbol{u} \cdot \nabla \boldsymbol{S}_0 + (\nabla \boldsymbol{u})^T \cdot \boldsymbol{S}_0 + \boldsymbol{S}_0 \cdot \nabla \boldsymbol{u}) \cdot \boldsymbol{u} \, \mathrm{d}V. \tag{14c}$$

The term

$$Q_{ps} = De_0 \int \nabla \cdot \frac{1}{f_0} (-\boldsymbol{u}_0 \cdot \nabla \boldsymbol{S} + (\nabla \boldsymbol{u}_0)^T \cdot \boldsymbol{S} + \boldsymbol{S} \cdot \nabla \boldsymbol{u}_0) \cdot \boldsymbol{u} \, \mathrm{d}V \tag{14d}$$

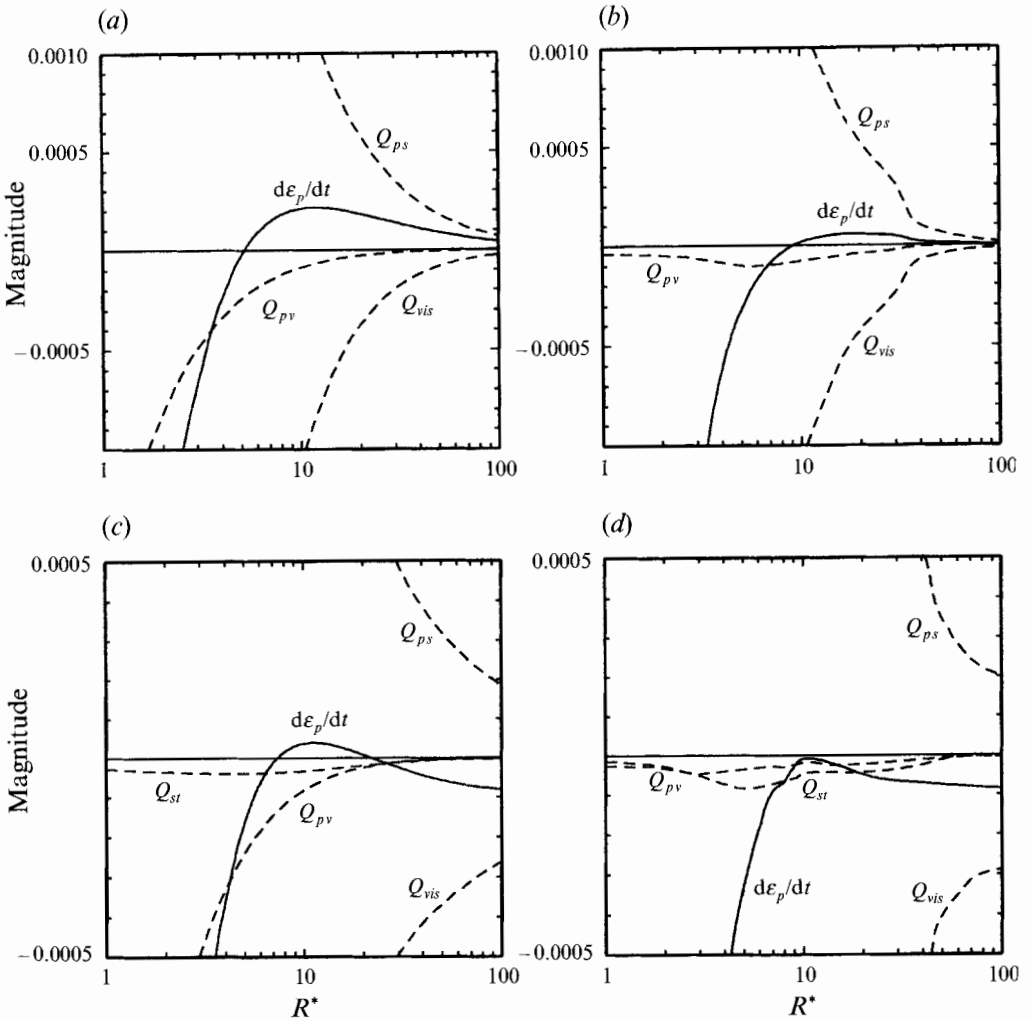

FIGURE 22. The terms ($Q_{vis}, Q_{pv}, Q_{ps}, Q_{st}, d\epsilon_p/dt$) in the energy analysis as a function of R^* for $\alpha = 3$, $\beta = 0.59$ and $De_0 = 2$ computed for the Oldroyd-B model ($L \to \infty$) for (*a*) axisymmetric disturbance and (*b*) and $m = 1$ non-axisymmetric disturbance, and for the modified Chilcott–Rallison model ($L = 60$) for (*c*) axisymmetric disturbance and (*d*) and $m = 1$ non-axisymmetric disturbance.

is the rate of energy caused by the coupling between the base flow field and disturbance polymeric stresses. Finally

$$Q_{st} = De_0 \int \nabla \cdot \delta_3 \operatorname{tr}(\boldsymbol{S})(-\boldsymbol{u}_0 \cdot \nabla \boldsymbol{S}_0 + (\nabla \boldsymbol{u}_0)^T \cdot \boldsymbol{S}_0 + \boldsymbol{S}_0 \cdot \nabla \boldsymbol{u}_0) \cdot \boldsymbol{u}\, dV \qquad (14e)$$

is the rate of energy transfer between the base and disturbance flows due to the shear-thinning terms in the MCR model. Following the argument of Joo & Shaqfeh (1992) for the inertialess disturbance momentum equation leads to a second relation for the time rate of change of ϵ_p given by

$$\frac{d\epsilon_p}{dt} = \beta \frac{d}{dt} \int \nabla \boldsymbol{u} : \nabla \boldsymbol{u}\, dV. \qquad (15)$$

Since $(\nabla \boldsymbol{u} : \nabla \boldsymbol{u})$ is a positive definite quantity, the sign of $d\epsilon_p/dt$ must indicate decay or

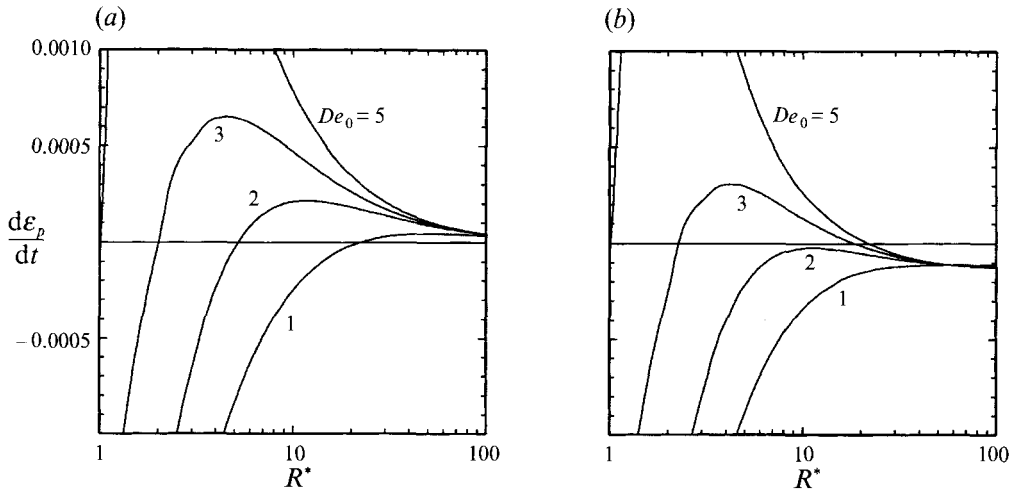

FIGURE 23. The total energy produced or dissipated by the axisymmetric disturbances as a function of R^* for $1 \leqslant De_0 \leqslant 5$ and for (*a*) $L \to \infty$ and (*b*) $L = 50$.

growth of the disturbances. To be more specific, energy is transferred from the mean flow to the disturbances (unstable configuration) or from disturbances to the mean flow (stable configuration) when $d\epsilon_p/dt$ has positive or negative signs, respectively. Although an identical mechanical energy approach to (14*a*)–(14*e*) can be obtained from the full Chilcott–Rallison model, a relationship of the form in (15) cannot be obtained because terms of the form Df/Dt enter the disturbance equations and prevent the development of a simple criterion for determining whether the base flow is stable or unstable.

The terms in the energy equation for axisymmetric and ($m = 1$) non-axisymmetric disturbances are plotted as a function of R^* in figure 22 for $De_0 = 2$ and $\beta = 0.59$ for the Oldroyd-B model ($L \to \infty$) and for the MCR model with $L = 60$. As expected, the magnitude of each term in (13) for the axisymmetric and non-axisymmetric disturbance flow is reduced when shear-thinning in the elastic normal stress is introduced since $f_0 > 1$; however, the sign of each contribution remains unchanged. The terms due to the coupling between the base state polymeric stresses and the axisymmetric and non-axisymmetric disturbance flow (Q_{pv}) dissipate energy for both models. The energy production caused by the coupling between the base state velocity field and the disturbance polymeric stress (Q_{ps}) is the primary instability mechanism for both axisymmetric and non-axisymmetric disturbances. The shear-thinning term (Q_{st}) results in additional energy dissipation for both axisymmetric and non-axisymmetric disturbances and becomes very small for $R^* \gg 1$, as shown in figures 22(*c*) and 22(*d*). In the Oldroyd-B model, energy is produced by the axisymmetric and non-axisymmetric disturbances above the critical value of R^* and the base flow remains unstable for $R^* > R^*_{crit}$. However, in the MCR model with $L = 60$, disturbance energy is produced by the axisymmetric disturbances ($m = 0$) only for values of R^* between $R^*_{1crit}(\alpha_{1crit}) < R^* < R^*_{2crit}(\alpha_{2crit})$. For non-axisymmetric disturbances with $m = 1$, the shear-thinning effects are strong enough for the base flow to remain stable at all radii for $L = 60$. In other words, for $De_0 = 2$, the rate of change of energy dissipation in the $m = 1$ non-axisymmetric disturbances is negative, as shown in figure 22(*d*) and the disturbance is damped everywhere.

The radial variation in the rate of change of total energy produced or dissipated by

axisymmetric disturbances is plotted in figure 23 as a function of De for the Oldroyd-B model and the MCR model with $L = 50$. From figure 23(*a*) it is clear that the total disturbance energy rate increases and the flow becomes unstable at progressively smaller values of the radius $R^* = R^*_{crit}$ as De_0 increases for the Oldroyd-B model. The total rate of change of disturbance energy generation passes through a maximum and asymptotes to very small positive values for large values of R^*, but never becomes negative again for $R^* > R^*_{crit}$ for each value of De_0. The power dissipated by the disturbance thus increases as it travels across the disk. In contrast, for the MCR model, the total energy produced by axisymmetric disturbances is reduced and $\mathrm{d}\epsilon_p/\mathrm{d}t$ tends to a negative value for $R^* \gg 1$.

5. Discussion

The evolution of the disturbances and the shape of the neutral stability diagrams predicted by the linear stability analysis of the nonlinear Chilcott–Rallison model are consistent with our experimental observations. Most importantly, we have shown that for a given solvent viscosity ratio β and finite dumb-bell extensibility L in the Chilcott–Rallison model, the elastic flow instability is limited to an annular ring near the centre of the disks. The instability develops at the critical radius $R^* = R^*_{1crit}(\alpha_{1crit})$ and the secondary motion propagates radially outward as travelling spiral waves when the Deborah number exceeds the critical Deborah number for the onset of instability. This disturbance flow dies out at a second, larger critical radius $R^* = R^*_{2crit}(\alpha_{2crit})$ and the flow becomes laminar, steady and purely azimuthal again. The secondary motions observed in the experiments for two different PIB/PB/C14 Boger fluids, with solvent viscosity ratios of $\beta = 0.59$ and $\beta = 0.84$, have the form of non-axisymmetric banded radial structures consisting of spiral vortices with a single well-defined wavelength.

The flow visualization results presented in this work provide a much clearer picture of the spatio-temporal structure of this purely elastic torsional flow instability than was obtained from the earlier work of McKinley *et al.* (1991*a*). At rotation rates just beyond the critical value and for short times after the onset of instability, a three-dimensional, time-dependent secondary flow with the form of outwardly travelling Archimedean spirals is observed across an annular region of the disks. The spatial characteristics of this secondary flow scale well with the rotation rate and the axial separation between the disks, and the radial wavelength of the most unstable mode remains approximately the same across the entire annular region, consistent with the predictions of the linear stability analysis. However, the experimentally observed flow instability is subcritical in the rotation rate, and at longer times the well-defined spiral secondary flow evolves into a more complicated motion consisting of complex three-dimensional spiral structures with a broad distribution of wavelength which may extend across the entire disk (cf. figure 13).

It should be noted that the travelling spiral structures observed in the experiments always have spiral numbers $m \leqslant 2$, and thus have azimuthal wavenumbers (m/R^*) which are much smaller than the radial wavenumber α. The spiral angle ϵ defined in (5) is thus typically small for this elastic instability. This is in sharp contrast to inertial instabilities near rotating disks where stationary spiral vortices with much higher spiral numbers of $m = 32$ are typically observed (Kobayashi, Kohama & Takamadate 1980). For the experimental conditions given in table 2, the typical spiral angle for the $m = 1$ mode is only $\epsilon \sim 5°$ and it is thus very difficult to distinguish whether the observed secondary motion is axisymmetric or not unless the full azimuthal planform of the disks is imaged. In addition, we find experimentally that the evolution of the spatial

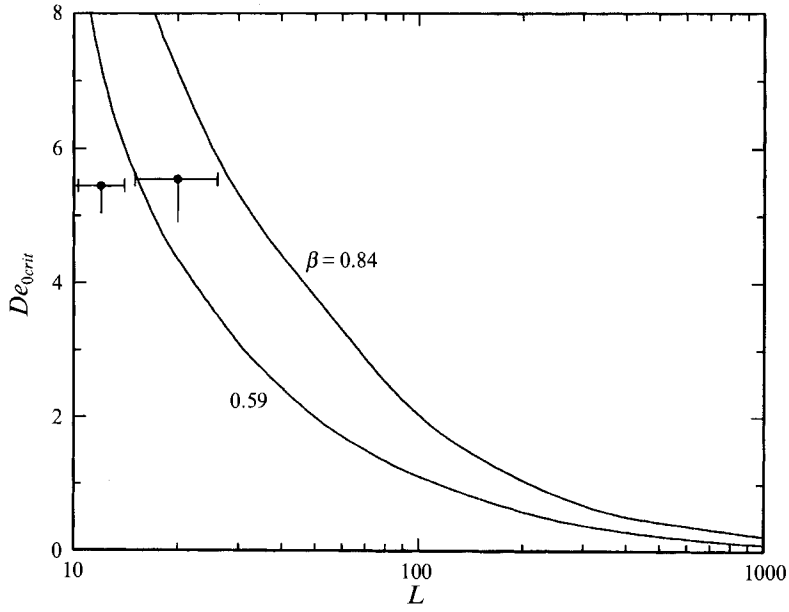

FIGURE 24. The critical Deborah number De_{0crit}, as a function of L for $\beta = 0.59$ and $\beta = 0.84$ predicted by experiments (●), and stability analysis (——), for the most dangerous instability mode.

and temporal characteristics of the disturbance are very different when large increments in the rotation rate $\delta\Omega$ beyond the critical value Ω_{crit} are applied. In particular, although we do not report on them here, we note that large step changes in Ω can result in the excitation of non-axisymmetric motions composed of inwardly travelling spiral waves which initiate at the outer edge of the geometry near the free surface and propagate radially inwards across the disks. Such modes can be readily identified in our earlier flow visualization studies (McKinley *et al.* 1991*a*). In order to observe only the most unstable monodisperse disturbances discussed in this work, careful control over the increments in Ω are required. Nonlinear analysis of three-dimensional, time-dependent disturbances will be required to capture the more complex flows that arise when large disturbances are applied to the base flow.

The agreement between experiment and theory for the prediction of the critical Deborah number is also greatly improved over the previous work of Öztekin & Brown (1993). In the limit $L \to \infty$ (corresponding to the quasilinear Oldroyd-B model), the present analysis for infinite disks predicts that the critical value of De_0 monotonically approaches zero, and the torsional flow is always unstable for any finite De_0 at large enough radii. However, when the magnitude of shear-thinning in the first normal stress coefficient is increased (by decreasing the extensibility parameter L), the positive spatial gradients in the normal stresses which provide the driving force of the elastic instability are decreased and the critical value of De_0 is increased. For quantitative comparison, the experimental values (with appropriate error bounds) and the prediction from the linear stability analysis for the critical Deborah number $De_0 = De_{0crit}(L)$ are shown in figure 24 for $\beta = 0.59$ and 0.84. The base flow remains stable everywhere for small values of De_0 for both values of β and all finite values of L. For a fixed viscosity ratio, the numerical value of the critical Deborah number is dependent on the exact value of the extensibility parameter L, which is determined experimentally from the best fit to the shear-rate-dependent first normal stress coefficient $\Psi_1(\dot{\gamma})$ of the PIB/PB/C14 elastic liquids. The steep slopes of the numerically calculated curves in figure 24 for

$L \leqslant 50$ signify how sensitive the critical Deborah number De_{0crit} is to changes in this extensibility parameter. This parameter can only be determined approximately from the steady-shear rheological data available (cf. figure 3) and some discrepancy between the data and computations in figure 24 is to be expected. In addition it should be noted that the experimental values of De_{0crit} determined from the growth of finite-amplitude perturbations to the base flow underpredict the linear stability calculations, as expected for a flow instability with a subcritical bifurcation structure. Both the experimental observations and the numerical calculations shown in figure 24 also indicate that the degree of stabilization by shear-thinning in the first normal stress coefficient is stronger for the higher solvent viscosity ratio. Similar stabilizing effects were demonstrated by Larson *et al.* (1994) using the K-BKZ model, and physically arise from the increased damping of the disturbance energy that is obtained when the relative contribution of the Newtonian solvent viscosity is increased. Numerical calculation is not continued for Deborah numbers beyond $De_0 = 8$ because the critical onset radius of the disturbances becomes very small. Since the present analysis is restricted to radially localized disturbances, it becomes unreliable when the onset radius of the instabilities becomes too small.

The predictions from the linear stability analysis for the axisymmetric and the $m = 1$ and $m = 2$ spiral vortices show that the difference in the critical onset radii for these modes is very small for elastic fluids with $\beta = 0.59$ or $\beta = 0.84$ and for the most physically realistic values of the parameter L. It is therefore likely that both axisymmetric and non-axisymmetric vortices will be observed simultaneously in experiments. In fact, both our current flow visualization experiments and previous observations by McKinley *et al.* (1991*a*) show the existence of several modes once the disturbances reach finite amplitude. Even close to the onset point of the instability, it is found that both the axisymmetric ($m = 0$) and the non-axisymmetric ($m = 1, m = 2$) spiral vortices can be observed in different experiments for slightly different values of the Deborah number, as indicated in table 2. For a solvent viscosity ratio of $\beta = 0.59$, the linear stability analysis predicts the $m = 1$ non-axisymmetric mode is always the most critical. However, for most values of the extensibility parameter L, the difference in the calculated onset radii of the axisymmetric and $m = 1$ and $m = 2$ spiral vortices are very small, as shown in figure 20.

Both the axisymmetric and non-axisymmetric spiral waves observed in the experiments correspond to vortices with dimensional radial spacing of approximately twice the gap between the plates, in good agreement with the calculations. The experimentally measured radial spacing between two bright regions at a constant value of θ corresponds to the wavelength $2\pi/\alpha$ described by the normal mode representation of the disturbances (equation (4)). A similar representation has been used for the flow of Newtonian fluids over a rotating disk to compare the predictions for spiral angle between experiments and calculations of the inertial instability, which gives rise to Ekman spirals (Kobayashi *et al.* 1980; Malik 1986). Both the measured and the calculated wavenumbers of the axisymmetric and non-axisymmetric disturbances exhibit a weak dependence on De_0 and β: the measured wavenumbers for different values of De_0 and β are $3.64 \leqslant \alpha \leqslant 4.11$, and the calculated wavenumbers vary in the range $3 \leqslant \alpha \leqslant 4$ for a broad range of De_0 and β. The wavenumbers from both the experiments and the analysis increase slightly as β increases.

The dimensionless radial wavespeed of the disturbances observed in the experiments remains approximately unchanged across the annular region of secondary flow, and is measured to be $c_r \approx 0.23$ for both the axisymmetric mode and spiral vortices in both PIB/PB/C14 Boger fluids, as shown in table 2. The linear stability analysis for the

axisymmetric mode ($m = 0$) predicts that the wavespeed of the disturbance depends on both the Deborah number and the radial location R^* being considered. For a fixed value of $De_0 = 5.5$, the radial wavespeed is approximately 0.08 when instability starts at $R^* = R^*_{1crit}(\alpha_{1crit})$ and is about 0.25 when disturbances decay again at $R^* = R^*_{2crit}(\alpha_{2crit})$. These values are relatively insensitive to the azimuthal form of the disturbance. For example, the calculated values of the critical wavespeed are 0.07 and 0.19 for spiral vortices with a winding number $m = 1$. The agreement between the experiments and the analysis is therefore good at larger radii. In fact, the comparison of the wavespeeds predicted by experiments and analysis for the Oldroyd-B model is equally good if the calculations are carried out at Deborah numbers based on the 'apparent relaxation time', $De = De(\dot{\gamma})$, evaluated at the local shear rate between the plates. The wavespeed of the axisymmetric instability for the Oldroyd-B fluid model with a solvent viscosity ratio $\beta = 0.59$ is calculated to be $c_r = 0.18$ using a Deborah number corresponding to the local shear rate at $R^* = R^*_{1crit}(\alpha_{1crit}) = 3.5$ (Öztekin & Brown 1993).

The critical values of the radii $R^* = R^*_{1crit}(\alpha_{1crit})$ and $R^* = R^*_{2crit}(\alpha_{2crit})$ defining the annular region of the unsteady flow determined from the experiments and stability calculations are shown in figures 25(*a*) and 25(*b*) for solvent viscosity ratios of $\beta = 0.59$ and $\beta = 0.84$, respectively. The observations and the calculations with the Chilcott–Rallison constitutive model are in qualitative agreement. Both show that the axisymmetric and spiral vortices are confined to an annular region bounded by R^*_{1crit} and R^*_{2crit}; however, the stability analysis consistently predicts lower values of these critical radii. Since our experimental observations of secondary motions are inherently finite in amplitude we expect them to result in an overestimation of R^*_1; similarly, outwardly travelling disturbances of finite amplitude may be expected to decay more slowly than infinitesimal perturbations and the decay radius R^*_2 will thus also be overestimated by the experiments. Closer comparison between theory and experiment requires nonlinear calculations of the finite-amplitude states or the incorporation of a more complex constitutive model with a spectrum of time constants which better describes the steady and transient material functions of the elastic test fluids (cf. figure 3). The systematic differences between the experimental measurements and the numerical predictions also may result from considering only radially localized disturbances. Since the disturbances are confined to a finite annular region for the Chilcott–Rallison model, the validity of this assumption is easier to justify than it is in the Oldroyd-B model for which the instabilities occur in an infinite domain. However, rigorous removal of this assumption requires consideration of the fully two-dimensional non-separable eigenvalue problem in the (r, z)-plane for each spiral mode.

Experiments spanning a wider range of aspect ratios (R/H) and solvent viscosity ratios (β) are desirable; however, the range of parameters experimentally attainable are constrained by a number of physical considerations. For disks with a given radius R, larger aspect ratios correspond to vortices of a smaller wavelength which are difficult to resolve spatially. Furthermore, for very small gap separations, the region of unsteady flow given by dimensionless radii in the range $R^*_{1crit} \leqslant R^* \leqslant R^*_{2crit}$ would physically correspond to a very narrow annular ring close to the centre of the disk. The elastic instability will still be present, but the contribution of the secondary flow to integrated measurements of the torque and normal force on the plates will be negligible. On the other hand, for larger gap separations the surface tension of the fluid is insufficient to overcome centrifugal and gravitational body forces and the sample will be flung out of the gap between the plates. The range of viscosity ratios η_s/η_0 physically realizable with Boger fluids also is limited. If the polymer concentration is increased in order to

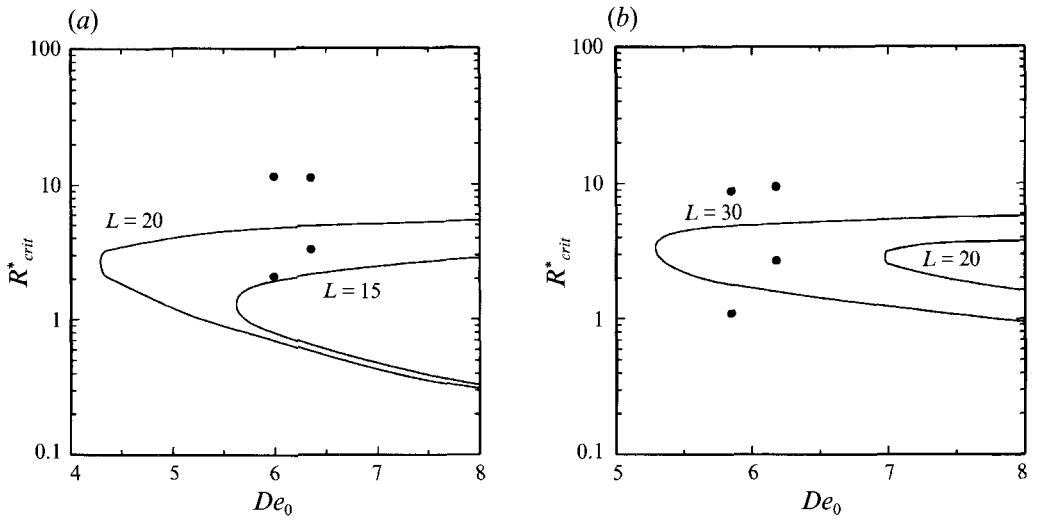

FIGURE 25. The critical onset radius $R^* = R^*_{crit}(\alpha_{crit})$ of the most dangerous mode as a function of De_0 predicted by experiments (●), and stability analysis (——), for the viscosity ratios of (*a*) $\beta = 0.59$ and (*b*) $\beta = 0.84$.

increase the relative contribution of η_p then the polymer solution crosses over from the dilute to the entangled regime, and stabilizing effects such as a non-zero value of the second normal stress coefficient Ψ_2 and pronounced shear-thinning in the viscosity become dominant. This typically constrains the solvent contribution to be greater than $\beta \geqslant 0.50$. Reducing the polymeric contribution to the viscosity below $\eta_p \approx 0.1\eta_0$ leads experimentally to very dilute non-entangled solutions with short relaxation times, whereas the numerical stability calculations show that larger values of β result in increasing stabilization of the base circumferential flow (cf. figure 25). It thus becomes difficult experimentally to achieve sufficiently high rotation rates and/or Deborah numbers to observe this torsional flow instability.

The results of the disturbance-energy analysis conclusively show that the instability mechanism for both axisymmetric and non-axisymmetric disturbances is similar for both a typical shear-rate-dependent nonlinear constitutive model and a simpler quasilinear model which predicts constant viscometric properties. The terms arising from the nonlinear coupling between the base state velocity field and the disturbance polymeric stresses control the onset of the purely elastic instability, and the rate of energy generated in these disturbances is reduced with increasing importance of shear-thinning in the extra hoop stress $S_{0\theta\theta}$. In the limit $L \to \infty$, a micromechanical description of the instability mechanism can be obtained by considering the infinitely extensible dumb-bells from which the Oldroyd-B constitutive equation is derived (Bird *et al.* 1987*b*), and by using arguments similar to the ones described by Öztekin & Brown (1993) for viscoelastic flow between parallel rotating disks and by Larson *et al.* (1990) and by Joo & Shaqfeh (1992) for viscoelastic Taylor–Couette flow. The mechanism of the instability is associated with the disturbance and base state polymeric stresses and the velocity gradients in the z- and θ-directions, which couple through the curved streamlines of the base flow to create a perturbation in the hoop stress, $S_{\theta\theta}$, that subsequently reinforces the disturbance. Joo & Shaqfeh (1994) have pointed out that the mechanisms for axisymmetric and non-axisymmetric instabilities in Taylor–Couette flows of the Oldroyd-B model differ slightly in the pathway that generates the disturbance hoop stress. The disturbance energy analysis presented here

shows that the instability mechanism for the more complex modified Chilcott–Rallison (MCR) model is very similar except that finite extensibility of the dumb-bells serves to reduce the magnitude of the destabilizing coupling between the base state kinematics and disturbance stresses and also gives rise to an additional dissipative contribution to the mechanical energy balance of the disturbance flow which restabilizes the purely circumferential torsional flow for large radii $R^* \gg 1$.

Since the mechanism of this elastic instability is similar to that observed in the elastic Taylor–Couette and Taylor–Dean instabilities (Larson *et al.* 1990; Joo & Shaqfeh 1994), it is not surprising that the spatio-temporal dynamics are also similar. In particular, these instabilities also have the form of periodic vortices with a single wavenumber for times shortly after onset, while at longer times nonlinear effects lead to a finer-scale structure. Our video-imaging results clearly show that non-axisymmetric modes are often the most unstable modes that are observed experimentally. It has been conjectured that the onset of similar non-axisymmetric modes explains the discrepancy between experimental and calculated critical Deborah numbers in the Taylor–Couette geometry (Larson *et al.* 1994; Avgousti & Beris 1993).

Although the analysis predicts that the difference in the onset radius of the radially inward-travelling negative angle and outward-travelling positive angle spiral vortices is very small, only positive angle spirals are observed by flow visualization at the linear stage of the instability. This is probably due to the fact that negative angle spirals travel radially inwards to smaller radii where the analysis suggests the base flow is linearly stable to all disturbances of spiral form. Any small disturbances which can be represented in this form will therefore be damped so that their amplitudes are never large enough to be detected in the experiments. However, it is obvious from figures 5(*e*) and 5(*f*) that negative angle spiral vortices are observed in the nonlinear motions observed at longer times. These structures propagate radially inward toward the centre of the disk and probably reflect back from the centre. The nonlinear interactions between these reflected waves and other travelling waves make the flow too complicated to decompose into discrete disturbance modes.

The results of these experiments and the associated stability analysis clearly indicate that the instabilities described here are responsible for the anti-thixotropic transition seen in the parallel rotating-disk rheometer. The onset of flow instabilities such as those shown here have important implications to measurements of the rheological properties of elastic liquids using a parallel-plate rheometer. In particular, it is clear from figure 5 that just beyond the critical Deborah number the time-dependent, three-dimensional secondary motion for a viscoelastic fluid with shear-rate-dependent elastic properties is confined to a narrow annular region near the centre of the geometry, and will thus be completely overlooked from direct observations of the free surface or meniscus shape. The same type of instability is also responsible for the similar flow transitions observed by us and other authors in a cone-and-plate rheometer. However, in this latter geometry, the viscometric shear flow between a conical disk and a flat plate is homogeneous, and thus the shear rate is constant everywhere across the disk. The secondary motion resulting from rotational flow instabilities therefore is not radially localized but extends throughout the sample for rotation rates beyond a critical Deborah number. Experimental and theoretical descriptions of the spatial and temporal characteristics of this instability will be reported in a later paper.

G.H.M. would like to thank the Merck Fund and the ACS-Petroleum Research Fund for the support of the experimental section of this work. The efforts of the other authors were supported by the Fluid Mechanics and Hydraulics Program of the NSF.

Appendix. Numerical solution

Equations (9)–(11) describe an eigenvalue problem for the growth rate σ and the eigenfunction, composed of the axial velocity $V(z)$, the vorticity $\omega(z)$ and polymeric stress components as a function of the spatial wavenumbers (α, m), the dimensionless radial distance R^* and the parameters L, De_0 and β. This eigenvalue problem is solved by discretization using Chebyshev polynomials.

The components of the eigenfunction are expanded in truncated series of Chebyshev polynomials. These expansions are simplified by transforming the computational domain $0 \leqslant z \leqslant 1$ to $\zeta = 2z+1$, so that the new variable ζ satisfies $-1 \leqslant \zeta \leqslant +1$. The transformed eigenvalue problems is solved using the mixed Tau and Galerkin technique (Gottlieb & Orszag 1977; Zebib 1987), in which the highest derivatives of the components of the eigenfunction corresponding to the disturbances in the axial velocity and $\omega(\zeta)$, and the eigenfunctions corresponding to the disturbance polymeric stress components are approximated by truncated sums of Chebyshev polynomials of the form

$$\begin{bmatrix} D^4W(\zeta) \\ D^2\omega(\zeta) \\ S_{rr}(\zeta) \\ S_{r\theta}(\zeta) \\ S_{rz}(\zeta) \\ S_{\theta\theta}(\zeta) \\ S_{\theta z}(\zeta) \\ S_{zz}(\zeta) \end{bmatrix} = \sum_{i=0}^{N} \begin{bmatrix} A_{1i} \\ A_{2i} \\ A_{3i} \\ A_{4i} \\ A_{5i} \\ A_{6i} \\ A_{7i} \\ A_{8i} \end{bmatrix} T_i(\zeta), \tag{A 1}$$

where T_i is the ith Chebyshev polynomial and the coefficients A_{ji} are computed as the solution of the algebraic eigenvalue problem. Representations of lower-order derivatives of velocity and $\omega(\zeta)$ are computed by integrating the terms of (A 1) related to the velocity and $\omega(\zeta)$ and using standard properties of Chebyshev polynomials. The integration constants are computed using the boundary conditions (11*a*)–(11*f*). Representations of the higher-order derivatives of polymeric stress components entering (10*a*)–(10*f*) are found by differentiation of the polynomial expansion of polymeric stress components in (A 1). The mixed Galerkin–Tau procedure reduces the system of equations and boundary conditions to a generalized matrix eigenvalue problem of the form

$$(\boldsymbol{A} + \sigma \boldsymbol{B})\, \boldsymbol{x} = \boldsymbol{0}, \tag{A 2}$$

where σ is the temporal eigenvalue, $\boldsymbol{x} \in \Re^{8(N+1)}$ are the components of the discretized eigenvector and the elements of the square matrices $\boldsymbol{A}$ and $\boldsymbol{B}$ each in $\Re^{8(N+1)\times 8(N+1)}$, depend on $(\alpha, m, L, De_0, R^*, \beta)$. Since the equations for axial velocity and $\omega(\zeta)$ do not involve the temporal eigenvalue σ, $\boldsymbol{B}$ has $2\times(N+1)$ rows of zeros and is therefore singular. The solution of (A 2) then will lead to $2\times(N+1)$ infinite eigenvalues. The method developed by Goussis & Pearlstein (1989) maps the infinite eigenvalues to one or more specified points in the complex plane without modifying the finite eigenvalues. The resulting eigenvalue problem is

$$(\boldsymbol{E} + \sigma \boldsymbol{F})\, \boldsymbol{x} = \boldsymbol{0}, \tag{A 3}$$

where $\boldsymbol{E} \in \Re^{8(N+1)\times 8(N+1)}$, and $\boldsymbol{F} \in \Re^{8(N+1)\times 8(N+1)}$ are written as partitioned matrices

$$\boldsymbol{E} = (\boldsymbol{H}, \boldsymbol{GP})^T, \quad \boldsymbol{F} = (\boldsymbol{B}^*, \boldsymbol{P})^T, \tag{A 4}$$

where $\boldsymbol{H} \in \Re^{6(N+1)\times 8(N+1)}$ and $\boldsymbol{P} \in \Re^{2(N+1)\times 8(N+1)}$ are the parts of the $\boldsymbol{A}$ matrix $\boldsymbol{A} \equiv (\boldsymbol{H}, \boldsymbol{P})^T$, $\boldsymbol{B} \equiv (\boldsymbol{B}^*, \boldsymbol{O})^T$, $\boldsymbol{O} \in \Re^{2(N+1)\times 8(N+1)}$ is the zero matrix, $\boldsymbol{B}^* \in \Re^{6(N+1)\times 8(N+1)}$ contains the non-zero parts of the $\boldsymbol{B}$ matrix, and $\boldsymbol{G}$ is a diagonal matrix of order $2\times(N+1)$ with elements $g_{ii} \equiv \epsilon_i$ and the coefficients ϵ_i are arbitrary constants. The eigenvectors and eigenvalues of the algebraic eigenproblems, (A 3), are computed using the algorithm available as DGVCCG in the IMSL library.

REFERENCES

AVGOUSTI, M. & BERIS, A. N. 1993 Nonaxisymmetric modes in viscoelastic Taylor–Couette flow. *J. Non-Newtonian Fluid Mech.* **50**, 225–251.

BIRD, R. B., ARMSTRONG, R. C. & HASSAGER, O. 1987*a* *Dynamics of Polymeric Liquids. Volume 1: Fluids Mechanics, 2nd edn.* Wiley Interscience.

BIRD, R. B., CURTISS, C. F., ARMSTRONG, R. C. & HASSAGER, O. 1987*b* *Dynamics of Polymeric Liquids. Volume 2: Kinetic Theory, 2nd edn.* Wiley Interscience.

BOGER, D. V. 1977/78 A highly elastic constant-viscosity fluid. *J. Non-Newtonian Fluid Mech.* **3**, 87–91.

CHIAO, S.-M. F. & CHANG, H.-C. 1990 Instability of a Criminale–Ericksen–Filbey fluid in a disk-and-cylinder system. *J. Non-Newtonian Fluid Mech.* **36**, 361–394.

CHILCOTT, M. D. & RALLISON, J. M. 1988 Creeping flow of dilute polymer solutions past cylinders and spheres. *J. Non-Newtonian Fluid Mech.* **29**, 381–432.

COATES, P. J., ARMSTRONG, R. C. & BROWN, R. A. 1992 Calculation of steady state viscoelastic flow through axisymmetric contractions with the EEME formulation. *J. Non-Newtonian Fluid Mech.* **42**, 141–188.

CREWTHER, I., HUILGOL, R. R. & JOZSA, R. 1991 Axisymmetric and nonaxisymmetric flows of a non-Newtonian fluid between coaxial rotating disks. *Phil. Trans. R. Soc. Lond.* A **337**, 467–495.

DAVIS, P. J. 1993 *Spirals: From Theodorus to Chaos.* A. K. Peters. Wellesley, MA.

FERRY, J. D. 1980 *Viscoelastic Properties of Polymers*, 3rd edn. Wiley Interscience.

FLORY, P. J. 1953 *Principles of Polymer Chemistry.* Cornell University Press.

GIESEKUS, H. 1965 Sekundärsrömungenin Viskoelastischen Flüssigkeiten bei Stationärer und Periodischer Bewegung. *Rheol. Acta* 4, 85–101.

GOTTLIEB, D. & ORSZAG, S. A. 1977 *Numerical Analysis of Spectral Methods: Theory and Applications.* Society for Industrial and Applied Mathematics, Bristol, UK.

GOUSSIS, D. A. & PEARLSTEIN, A. J. 1989 Removal of infinite eigenvalues in the generalized matrix eigenvalue problem. *J. Comput. Phys.* **84**, 242–246.

GRIFFITHS, D. F., JONES, D. T. & WALTERS, K. 1969 A flow reversal due to edge effects. *J. Fluid Mech.* **36**, 161–175.

HILL, C. T. 1972 Nearly viscometric flow in the disk and cylinder system. II: Experimental. *Trans. Soc. Rheol.* **16**(2), 213–245.

HUTTON, J. F. 1969 Fracture and secondary flow of elastic liquids. *Rheol. Acta* **8**(1), 54–59.

JACKSON, J. P., WALTERS, K. & WILLIAMS, R. W. 1984 A rheometrical study of Boger fluids. *J. Non-Newtonian Fluid Mech.* **14**, 173–188.

JI, Z., RAJAGOPAL, K. R. & SZERI, A. Z. 1990 Multiplicity of solutions in von Kármán flows of viscoelastic fluids. *J. Non-Newtonian Fluid Mech.* **36**, 1–25.

JOO, Y. L. & SHAQFEH, E. S. G. 1991 Viscoelastic Poiseuille flow through a curved channel: a new elastic instability. *Phys. Fluids* A **3**(7), 1691–1694.

JOO, Y. L. & SHAQFEH, E. S. G. 1992 A purely elastic instability in Dean and Taylor–Dean flow. *Phys. Fluids* A **4**(3), 524–543.

JOO, Y. L. & SHAQFEH, E. S. G. 1994 Observations of purely elastic instabilities in the Taylor–Dean flow of a Boger fluid. *J. Fluid Mech.* **262**, 27–73.

KOBAYASHI, R., KOHAMA, Y. & TAKAMADATE, C. 1980 Spiral vortices in boundary layer transition regime on a rotating disk. *Acta Mech.* **35**, 71–82.

LARSON, R. G. 1992 Instabilities in viscoelastic flows. *Rheol. Acta* **31**, 213–263.

LARSON, R. G., MULLER, S. J. & SHAQFEH, E. S. G. 1994 The effect of fluid rheology on the elastic Taylor–Couette flow instability. *J. Non-Newtonian Fluid Mech.* **51**, 195–225.

LARSON, R. G., SHAQFEH, E. S. G. & MULLER, S. J. 1990 A purely elastic instability in Taylor–Couette flow. *J. Fluid Mech.* **218**, 573–600.

LEE, C. S., TRIPP, B. C. & MAGDA, J. J. 1992 Does N_1 or N_2 control the onset of edge fracture. *Rheol. Acta* **31**, 306–398.

MCKINLEY, G. H., ARMSTRONG, R. C. & BROWN, R. A. 1993 The wake instability in viscoelastic flow past confined cylinders. *Phil. Trans. R. Soc. Lond.* **344**, 265–304.

MCKINLEY, G. H., BYARS, J. A., BROWN, R. A. & ARMSTRONG, R. C. 1991*a* Observations on the elastic instability in cone-and-plate and parallel-plate flows of a polyisobutylene Boger fluid. *J. Non-Newtonian Fluid Mech.* **40**, 201–229.

MCKINLEY, G. H., RAIFORD, W. P., BROWN, R. A. & ARMSTRONG, R. C. 1991*b* Nonlinear dynamics of viscoelastic flow in axisymmetric abrupt contractions. *J. Fluid Mech.* **223**, 411–456.

MAGDA, J. J. & LARSON, R. G. 1988 A transition occurring in ideal elastic liquids during shear flow. *J. Non-Newtonian Fluid Mech.* **30**, 1–19.

MAGDA, J. J., LOU, J., BAEK, S.-G. & DEVRIES, K. L. 1991 Second normal stress difference of a Boger fluid. *Polymer* **32**(11), 2000–2009.

MALIK, M. R. 1986 The neutral curve for stationary disturbances in rotating-disk flow. *J. Fluid Mech.* **164**, 275–287.

MERZKIRCH, W. 1987 *Flow Visualization*, 2nd edn. Academic.

MULLER, S. J., SHAQFEH, E. S. G. & LARSON, R. G. 1993 Experimental studies of the onset of oscillatory instability in viscoelastic Taylor–Couette flow. *J. Non-Newtonian Fluid Mech.* **46**, 315–330.

OLAGUNJU, D. O. 1994 Effect of free surface and inertia on viscoelastic parallel plate flow. *J. Rheol.* **38** (1), 151–168

ÖZTEKIN, A. & BROWN, R. A. 1993 Instability of a visoelastic fluid between rotating parallel disks: analysis for the Oldroyd-B fluid. *J. Fluid Mech.* **255**, 473–502.

PHAN-THIEN, N. 1983 Coaxial-disk flow of an Oldroyd-B fluid: exact solution and stability. *J. Non-Newtonian Fluid Mech.* **13**, 325–340.

PHAN-THIEN, N. 1985 Cone and plate flow of the Oldroyd-B fluids is unstable. *J. Non-Newtonian Fluid Mech.* **17**, 37–44.

PRILUTSKI, G., GUPTA, R. K., SRIDHAR, T. & RYAN, M. E. 1983 Model viscoelastic liquids. *J. Non-Newtonian Fluid Mech.* **12**, 233–241.

QUINZANI, L. M., MCKINLEY, G. H., BROWN, R. A. & ARMSTRONG, R. C. 1990 Modeling the Rheology of Polyisobutylene Solutions. *J. Rheol.* **34**(5), 705–748.

RUSS, J. C. 1992 *The Image Processing Handbook*. CRC Press, Boca Raton.

SHAQFEH, E. S. G., MULLER, S. J. & LARSON, R. G. 1992 The effects of gap width and dilute solution properties on the viscoelastic Taylor–Couette instability. *J. Fluid Mech.* **235**, 285–317.

STEIERT, P. & WOLFF, C. 1990 Rheological properties of a polyisobutylene in a kerosene/polybutene mixture in simple shear flow. *J. Non-Newtonian Fluid Mech.* **35**, 189–196.

TANNER, R. I. & KEENTOK, M. 1983 Shear fracture in cone-plate rheometry. *J. Rheol.* **27**(1), 47–57.

WALSH, W. P. 1987 On the flow of a non-Newtonian fluid between rotating co-axial disks. *Z. angew. Math. Phys.* **38**, 495–511.

ZANDBERGEN, P. J. & DIJKSTRA, D. 1987 Von Kármán swirling flows. *Ann. Rev. Fluid Mech.* **19**, 465–491.

ZEBIB, A. 1987 Removal of spurious modes encountered in solving stability problems by spectral methods. *J. Comput. Phys.* **70**, 521–525.